Can the magmatic conditions of the Martian nakhlites be discerned via investigation of clinopyroxene and olivine crystallographic slip-systems?

S. Griffin[1], L. Daly[1,2,3,4], S. Piazolo[5], L. V. Forman[2], B. E. Cohen[6], M. R. Lee[1], P. W. Trimby[7], R. J. Baumgartner[8,9], G. K. Benedix[2,10,11], and B. Hoefnagels.

[1]School of Geographical and Earth Sciences, University of Glasgow, UK.

[2]Space Science and Technology Centre, School of Earth and Planetary Sciences, Curtin University, Australia.

[3]Australian Centre for Microscopy and Microanalysis, The University of Sydney, Australia.

[4]Department of Materials, University of Oxford, UK.

[5]School of Earth and Environment, University of Leeds, UK.

[6]Department of Materials, University of Oxford, UK. 5School of Geosciences, University of Edinburgh, UK.

[7]Oxford Instruments Nano analysis, High Wycombe, UK.

[8]School of Biological, Earth and Environmental Sciences, The University of New South Wales, Kensington, NSW, Australia.

[9]CSIRO Mineral Resources, Australian Resources Research Centre, Kensington, WA, Australia.

[10]Department of Earth and Planetary Sciences, Western Australia Museum, Australia.

[11]Planetary Institute, USA.

Corresponding author: Sammy Griffin (Sammy.Griffin@glasgow.ac.uk)

Key Points:

- Large area EBSD reveals shock-derived deformation to mask non-shock deformation even in low deformation regions in the nakhlites.
- Slip-system patterns indicate nine distinct derived deformation signatures for the nakhlites, interpreted as shock-induced deformation.
- Non-shock derived slip-system patterns are identified within low deformation regions interpreted as emplacement deformation.

Abstract

Deformation is a near ubiquitous process that is observed within nearly all naturally forming rocks, terrestrial and extra-terrestrial. Large area electron backscatter diffraction (EBSD) is a technique that enables slip-systems (a form of plastic deformation) to be inferred at a comparable scale to representative texture analysis (≥100 crystals). Extensive laboratory and studies on naturally occurring samples have identified preferential extrinsic parameters for specific slip-system signatures within olivine and clinopyroxene for mantle conditions. Slip-systems in both olivine and augite (high Ca-clinopyroxene) for 21 large area EBSD datasets sourced from 16 different Martian nakhlite meteorites were analysed and assessed against these parameters. When investigating the high and low deformation regions within the samples 10 of the 21 sections exhibited a shift in the slip-system patterns between the low and high deformation regions. The secondary signatures identified within the low deformation regions are inferred to relate to emplacement deformation. Thus, these samples exhibit both shock and emplacement signatures. The observed variations in deformation patterns for the two main regimes of deformation indicate heterogeneous sampling of the nakhlite ejecta crater. Our findings indicate that shock deformation is prevalent throughout the nakhlites, and that great care needs to be taken when interpreting slip-deformation of crystals within apparent lower deformation regions.

Plain Language Summary

Clinopyroxene and olivine are important minerals for studying igneous processes on Mars and Earth (from the surface to the upper mantle). Here, clinopyroxene and olivine slip-system patterns - deformational movement within a crystal - were investigated using the specialist microscopic technique of electron backscatter diffraction (EBSD), which enables the identification of crystal structures within a group of Martian meteorites known as the nakhlites. The nakhlites are mafic rocks representing the largest collection of rocks from a singular – but as yet unknown – location on Mars. Combined slip-system patterns for both olivine and clinopyroxene reveal nine different shock deformation signatures for the nakhlites indicating that they were sourced from multiple locations within the ejection crater. Non-shock related deformation can also be observed but tends to be masked by the dominance of shock deformation features even in low deformation regions.

1 Introduction

Deformation within rocks is driven by a wide variety of geological processes *e.g.*, compaction (mountain building, subduction, burial), extension (rifting), shear (flow, faulting), and dramatic changes in both temperature (contact metamorphism, melting/recrystallisation, hypervelocity impacts, and hydrothermal activity) and pressure (hypervelocity impacts, rapid burial). Extrinsic parameters present over a rocks geological history will impact the way each crystal within the sample will grow and deform. Mineral deformation within rocks can occur via several mechanisms including elastic, brittle, and ductile deformation. Where ductile deformation including dislocation creep, diffusion creep, and dissolution-precipitation creep. Microstructures and defects (*e.g.*, dislocations) present within a mineral's crystal lattice record important information pertaining to its crystal plastic deformation (Ashby, 1970, 1983; Fleck et al., 1994; Poirier, 1975, 1985, 1995; Poirier & Nicolas, 1975; Sciences, 1978; Stocker & Ashby, 1973). Plastic deformation, a stress and or strain derived permanent change lacking brittle failure or volume change within a material, is typically accommodated at the nano-meter scale by

crystallographic slip or rotation. Crystallographic slip-systems are directional movement of either slip or rotation which occurs around specific crystallographic axes within either the crystal lattice, sub-boundaries, or inequant crystals (Law, 1990). Within geological specimens, plastic deformation has been shown to develop through either crystallisation processes e.g., mantle/flow rheology, growth twins, (Cordier, 2002; Fei et al., 2012; Frets et al., 2012; Henry et al., 2017; Yao et al., 2019; Zhang et al., 2006) and/or subsequent modification processes *e.g.*, metamorphic shear, mineralogical dehydration/degassing, compaction, or shock (Friedrich et al., 2017; Godard & van Roermund, 1995; van Roermund & Boland, 1981; Ruzicka & Hugo, 2018; Tasaka et al., 2008; Yao et al., 2019). The accumulation of these deformation microstructures, when combined across a representative area of a rock, produce a macroscale pattern of plastic deformation. This macroscale pattern is reported within geological samples as crystallographic preferred orientations (CPO) also known as lattice preferred orientation (LPO), which refers to the nature and extent of orientation of the crystal lattice axis with respect to a specific phase within the sample (Bernard et al., 2019; Hunter, 1996; Mainprice et al., 2015).

Previous studies of crystallographic dislocation systems, have shown an activation dependence of slip around specific crystallographic axes, when a crystal is exposed to a differential stress under varying extrinsic conditions *e.g.*, stress, strain, temperature, pressure, and water content (*e.g.*, Raterron and Jaoul, 1991; Katayama et al., 2004; Karato et al., 2008; Raterron et al., 2011; Bernard et al., 2019; Liu et al., 2019). Subsequently, by identifying and characterising the dominant crystallographic dislocation systems activated within particular minerals through extensive laboratory experiments and studies of naturally occurring samples, the ability to broadly ascertain the environment (pressure, temperature, stress, strain, and water content) parameters a rock experienced during deformation has started to develop which can be utilised to provide insight into a given sample's geological history (Barber et al., 2010). However, despite the wealth of information that is stored within crystallographic dislocations and the ever-increasing body of literature, there is a lot about these systems that yet to be fully utilised and understood.

Intrinsic controls (*e.g.*, chemistry) alongside extrinsic controls (*e.g.*, temperature, pressure, stress magnitude and strain rate) have long been recognised as important factors for the activation of crystallographic slip-systems in minerals (Ashby, 1983; Barber et al., 2010; Bernard et al., 2019; Groves & Kelly, 1963; Jaoul & Raterron, 1994; Müller et al., 2008; Poirier, 1982; Woodward, 2005). However, recent studies of olivine have shown that there are additional factors that can also influence the activation of a given slip-system (Barber et al., 2010; Bernard et al., 2019). These factors include the mechanism of deformation, water content, deformation geometry, presence of melt, and previous deformation history (Boneh & Skemer, 2014; Hansen et al., 2014; H. Jung et al., 2006; Haemyeong Jung et al., 2009; Katayama & Karato, 2006; Précigout & Hirth, 2014; Qi et al., 2018; Sundberg & Cooper, 2008). These other identified factors have the capacity to shift the previously identified activation boundaries of specific slip-systems, related to the minerals chemistry, and the local temperature, pressure, and time frame over which deformation occurs. This is why slip-systems observed in some naturally occurring samples show slip-system signatures at lower extrinsic values compared to those determined from laboratory experiments (Bernard et al., 2019).

Here the activation of crystallographic slip-systems within olivine and augite (high Ca-clinopyroxene; Fig. 1, 2), representatives of the orthorhombic and monoclinic crystal systems,

respectively, are assessed. Olivine has been extensively studied, both experimentally and in naturally occurring samples of mantle rocks, due to its high-abundance in the Earth's upper mantle which enables insight into the mantle's structure and seismic anisotropy (Bernard et al., 2019; Kaboli et al., 2017; Li et al., 2020; Mainprice et al., 2005; Mei & Kohlstedt, 2000; Poirier, 1975; Soustelle & Manthilake, 2017). Thus, the activation criteria for olivine's crystallographic slip-systems over a variety of extrinsic pressure, temperature, stress, strain, and water contents are fairly well constrained (Bernard et al., 2019; Karato et al., 2008; Katayama & Karato, 2006). Augite, on the other hand, is only starting to be studied in the same level of detail (Tedonkenfack et al., 2021; Van Der Werf et al., 2017). Previous work exploring slip-systems in clinopyroxene has predominantly focused on diopside (monoclinic with a similar crystal lattice structure to augite), but mostly in laboratory settings; many of the crystallographic slip-systems observed experimentally have not yet been observed within naturally occurring terrestrial rocks (Bascou et al., 2002; Bystricky & Mackwell, 2001; Ingrin et al., 1991; Jaoul & Raterron, 1994; Mauler et al., 2000; Skrotzki, 1994). However, studies focused on observing clinopyroxene crystallographic slip-systems and CPO in a natural occurring samples has started to increase (Keppler, 2018; Skrotzki, 1994; Tedonkenfack et al., 2021; Van Der Werf et al., 2017). From current limited knowledge of clinopyroxene crystallographic dislocation systems [often based off numerical simulations *e.g.*, Ulrich & Mainprice (2005)], there is a strong dependence on the mineral's orientation relative to the principal stress axes. Observations of clinopyroxene indicate that a dominant slip-system signature pairing dominant (100)[001] with minor (001)[100] (Fig. 2) will form under most Earth relevant extrinsic conditions (Kollé & Blacic, 1982; P. Raterron et al., 1994).

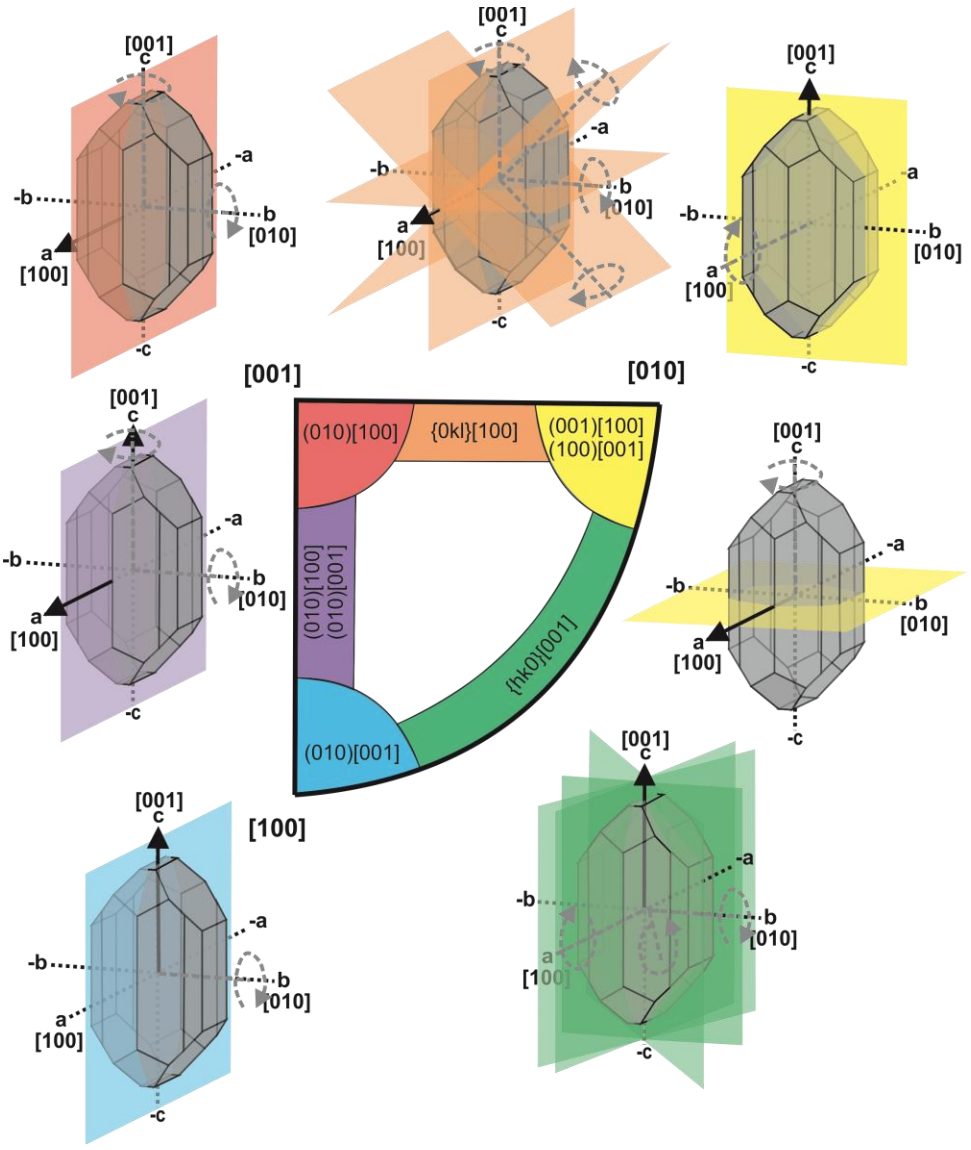

Figure 1. Olivine (forsterite; mmm; unit cell lengths a = 0.466, b = 1, c = 0.587) crystallographic slip-system signature key (notated as the slip plane and slip direction) expressed as the orthorhombic crystallographic fundamental sector [lowest form of crystal symmetry; modified from Ruzicka and Hugo (2018)]. The corners of the key refer to olivine's specific crystallographic axis (<a> = [100], <b> = [010], and <c> = [001]). The surrounding diagrams visualise the different slip planes where the straight black arrows indicate the direction of slip for both twist and tilt boundaries. For a tilt boundary [movement perpendicular (axis parallel) to the plane] the black arrows also indicate the tilt axis whereas the plane rotation axis for a twist (*i.e.*, rotating) boundary [movement within (axis perpendicular) to the plane] is indicated by the grey dashed arrows.

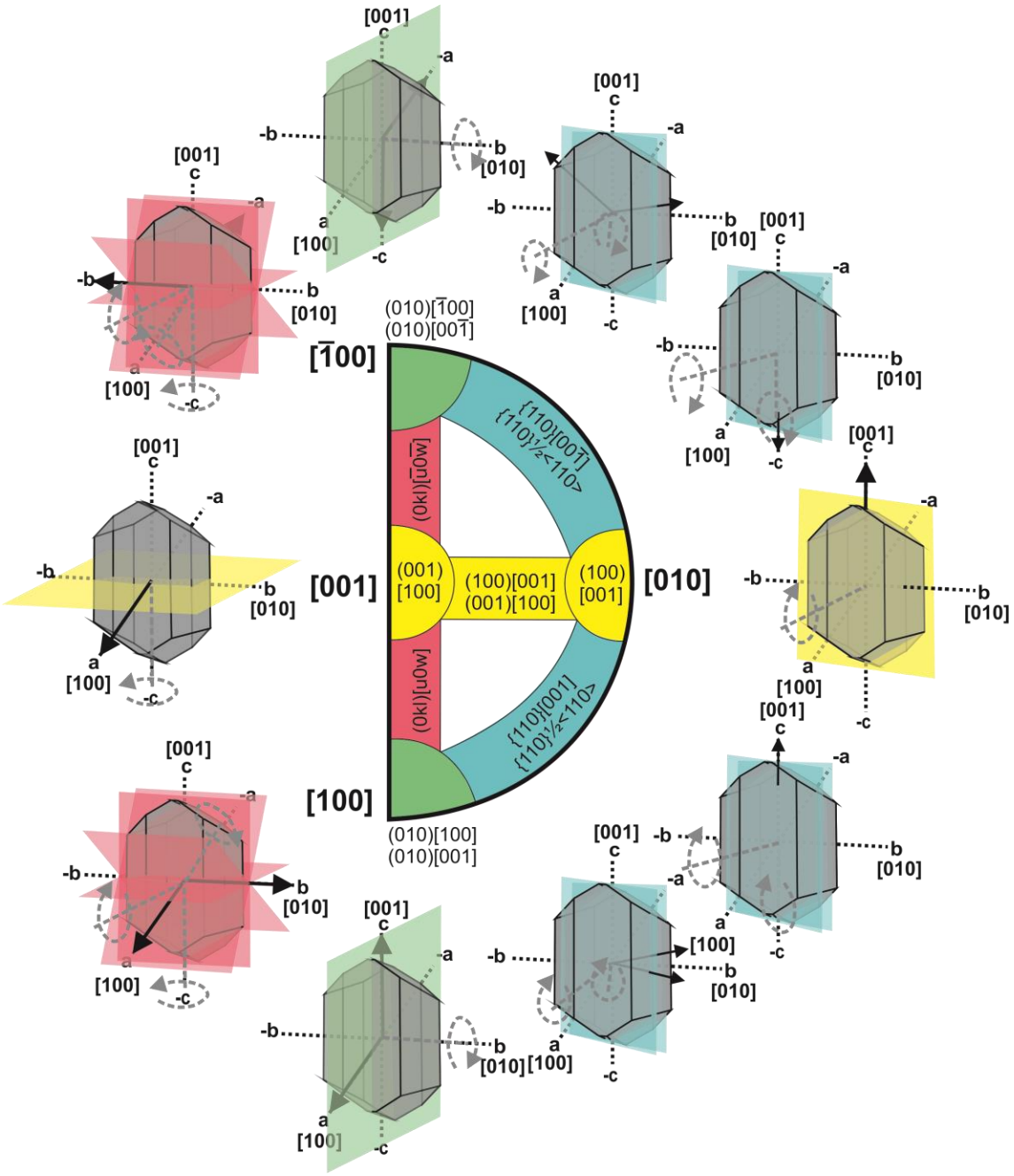

Figure 2. Augite (high Ca-clinopyroxene; 2/m; unit cell lengths a = 1.097, b = 1, c = 0.596) crystallographic slip-system signature key (notated as the slip plane and direction) expressed as the monoclinic crystallographic fundamental sector (lowest form of crystallographic symmetry). The outer bracketed labels of the key refer to augite's specific crystallographic axis (<a> = [100], <b> = [010], and <c> = [001]). The surrounding diagrams visualise the different slip planes where the straight black arrows indicate the direction of slip for both twist and tilt boundaries. For a tilt boundary [movement perpendicular (axis parallel) to the plane] the black arrows also indicate the tilt axis whereas the plane rotation axis for a twist (*i.e.*, rotating) boundary [movement within (axis perpendicular) to the plane] is indicated by the grey dashed arrows.

Most of the Martian meteorites that are available for study are mafic-ultramafic igneous rocks (Udry et al., 2020) and references therein. To date the Martian meteorites, consist of the clinopyroxene rich shergottites and nakhlites, orthopyroxenite ALH 84001, the dunitic chassignites, and a non-igneous group of polymict breccias. The nakhlites, which are the focus of this study, have average crystal-sizes ranging from 0.29–1 mm with a cumulate texture (Udry & Day, 2018), are ultramafic in composition derived from mafic parental magmas with low-moderate abundances of olivine (1.7–14.9 modal%) and high abundances of augite (55–71 modal%; (Udry & Day, 2018). The remaining 0–42 modal% of the nakhlites is mesostasis material (Udry & Day, 2018). The mesostasis material contains varying proportions of clinopyroxene, orthopyroxene, olivine, plagioclase, titanomagnetite, iron sulphides, and glass (Corrigan et al., 2015). The nakhlites are currently considered the largest group of Martian rocks sourced from a singular location on Mars, due to their consistent 10.7 ± 0.8 Ma ejection age (Cohen et al., 2017; Udry et al., 2020). They are also the least affected by shock [*i.e.,* high strain, maximum bulk shock pressures 5–20 GPa (Fritz, Artemieva, et al., 2005)], where shock deformation has been reported to occur as bands within the samples (Daly et al., 2019; Fritz, Artemieva, et al., 2005), potentially leaving regions that are more representative of low strain (mantle) deformation than high strain (shock) deformation. Nearly all of the meteorites within the group contain evidence of aqueous alteration on Mars in the form of iddingsite (Bunch & Reid, 1975; Hallis & Taylor, 2011; Krämer Ruggiu et al., 2020; Lee et al., 2015; Noguchi et al., 2009; Treiman, 2005; Udry et al., 2020), and have been shown to sample several temporally distinct igneous events that are geochemically related by a shared magma source region (Cohen et al., 2017; Day et al., 2018; Treiman, 2005; Udry et al., 2020). Recent specimen additions to the nakhlite group over the last decade have questioned the former hypothesised formation mechanism of the nakhlites [*i.e.,* a large cumulate lava flow on the surface of Mars (Treiman, 2005)]. This raises the question as to whether the nakhlites formed solely as lava flows, shallow (≤3 km depth) intrusions, or a combination of flows and intrusions.

Majority of the work on augite and olivine deformation has been focused on understanding mantle (*i.e.,* low strain rate -low stress – high temperature) conditions. However, due to the mechanism of nakhlite extraction by impact and ejection deformation in these meteorites is expected to contain high strain rate deformation in the form of shock metamorphism. This shock deformation. This shock deformation although reported to be low in comparison to other Martian meteorites (Fritz, Artemieva, et al., 2005), will have impacted and may have overprinted the magmatic deformation signatures within the nakhlites. Accordingly, in principle nakhlites are expected to carry signatures of both emplacement and ejection. This study asks: can crystallographic deformation parameters be used to further the understanding of rocky (planetary) bodies other than Earth, including the Moon, asteroids, and Mars? To tackle this question, crystal plastic deformation (slip-systems) of olivine and clinopyroxene within the nakhlites from Mars are investigated.

2 Materials and Methods

Twenty-one Large Area EBSD datasets were collected for this study, covering 16 individual nakhlite meteorites: Caleta el Cobre 022, Governador Valadares, Lafayette, Miller range (MIL) 03346, MIL 090030, MIL 090032, MIL 090136, Nakhla, Northwest Africa (NWA) 817, NWA 998, NWA 10153, NWA 11013, NWA 12542, Yamato (Y) 000593, Y 000749, Y 000802 (Table 1). The presented EBSD data includes all known ‘paired stones’ for the Miller

Range (MIL) and Yamato (Y) nakhlites. Two sections of five meteorites: Governador Valadares, Nakhla, Northwest Africa (NWA) 998, Y 000593, and Y 000749 were also analysed to assess the impact of experimental parameters as well as result consistency across different sections.

Each analysed thick section was coated with a ~10 nm thick conductive carbon coat using a sputter coater after undergoing both mechanical (iterative 1 µm followed by 0.3 µm aluminum spheres suspended in glycol for 5 minutes each) and chemical (4 hours using 0.1 µm colloidal silica suspended in a NaOH solution) polishing prior to EBSD analysis.

EBSD analyses were run using four different instruments in four different labs: ISAAC imaging centre, University of Glasgow (Zeiss Sigma Field Emission Gun Variable Pressure Scanning Electron Microscope (FEG-VP-SEM) with Oxford Instruments NordlysMax^2 EBSD detector, operating Oxford Instruments AZtec analysis software v3.3); Geochemical Analysis Unit (GAU), Macquarie University (Carl Zeiss IVO SEM using a HKL NordlysNano high Sensitivity EBSD detector); Oxford Instruments Nanoanalysis HQ, High Wycombe (Hitachi SU70 FEGSEM equipped with a Symmetry CMOS detector and indexed using AZtec analysis software v3.4); and the John de Laeter Centre, Curtin University (Tescan MIRA3 VP-FESEM with the NordlysNano EBSD detector and AZtec EDS/EBSD acquisition system). All analyses were run at 20 keV, 4–8 nA beam current, at a 70° tilt, under high vacuum (~3.4 x 10^8 Pa) apart from MIL 03346 (118) and Lafayette (USNM 1505-1), which were run at low vacuum (~49 Pa). Selected step sizes (ranging 0.4–15 µm) for each sample were chosen to maximise the area covered by the EBSD maps and ensure data collection over available timeframes whilst ensuring the MAD values, indicators of index quality, were <1 (all phases ranging 0.48–0.82; Table 1).

All EBSD datasets were processed using Oxford Instruments Channel 5 software. Crystallographic axes for the forsterite and augite phases were defined as b = 1 > c = 0.587 > a = 0.466 (forsterite) and a = 1.097 > b = 1 > c = 0.596 (augite). To remove erroneous data (i.e., mis-indexed and non-indexed data points) without generating significant artefacts within the datasets (Bestmann and Prior, 2003; Watt et al., 2006; Forman et al., 2016; Daly et al., 2019a; Forman et al., 2019) the data was first noise reduced using a wildspike correction followed by a consecutive 8–6 point nearest neighbour zero solution reductions. Crystal boundaries were defined as >10° internal crystallographic misorientation from the nearest-neighbour pixel. Mechanical twins were identified as 180° rotation around augite (100), (204), or (104) axes and 60° rotation around forsterite (011), (012), and (100) axes. Simple twin boundaries were also identified in augite as 180° rotation around augite (001).

Meteorites, such as the nakhlites presented here, lack any consistent external reference frame. Principal orientations have therefore been arbitrarily defined as Y = top–bottom direction of the thick section's polished surface, X = left–right direction of the thick section's polished surface, and Z = direction perpendicular to the plane of the thick section's polished surface. EBSD is a reference-frame based technique thus, assigning a pseudo-external reference frame for the samples will enable comparison across the samples and provide a semblance of consistency in the analysis across all of the datasets. Grain (*i.e.,* crystal) reference orientation distribution (GROD) angle maps were used to identify regions of high deformation and low deformation within each of the nakhlites. Once the identified regions were checked against local misorientation, inverse pole figure (IPF), Euler, and phase maps specific subsets were created. All slip-system diagrams [misorientation axis inverse pole figure (mIPF) plots] for high

deformation, low deformation, and whole section datasets have been contoured using the settings of a maximum multiple uniform density (MUD.; representing the density of data points) of 5 with 5° clustering and a half width of 15° for internal misorientation between adjacent pixels ranging 2–10°. Slip-systems present within each dataset were identified from the MUD distribution patterns within the mIPF plots.

3 Results

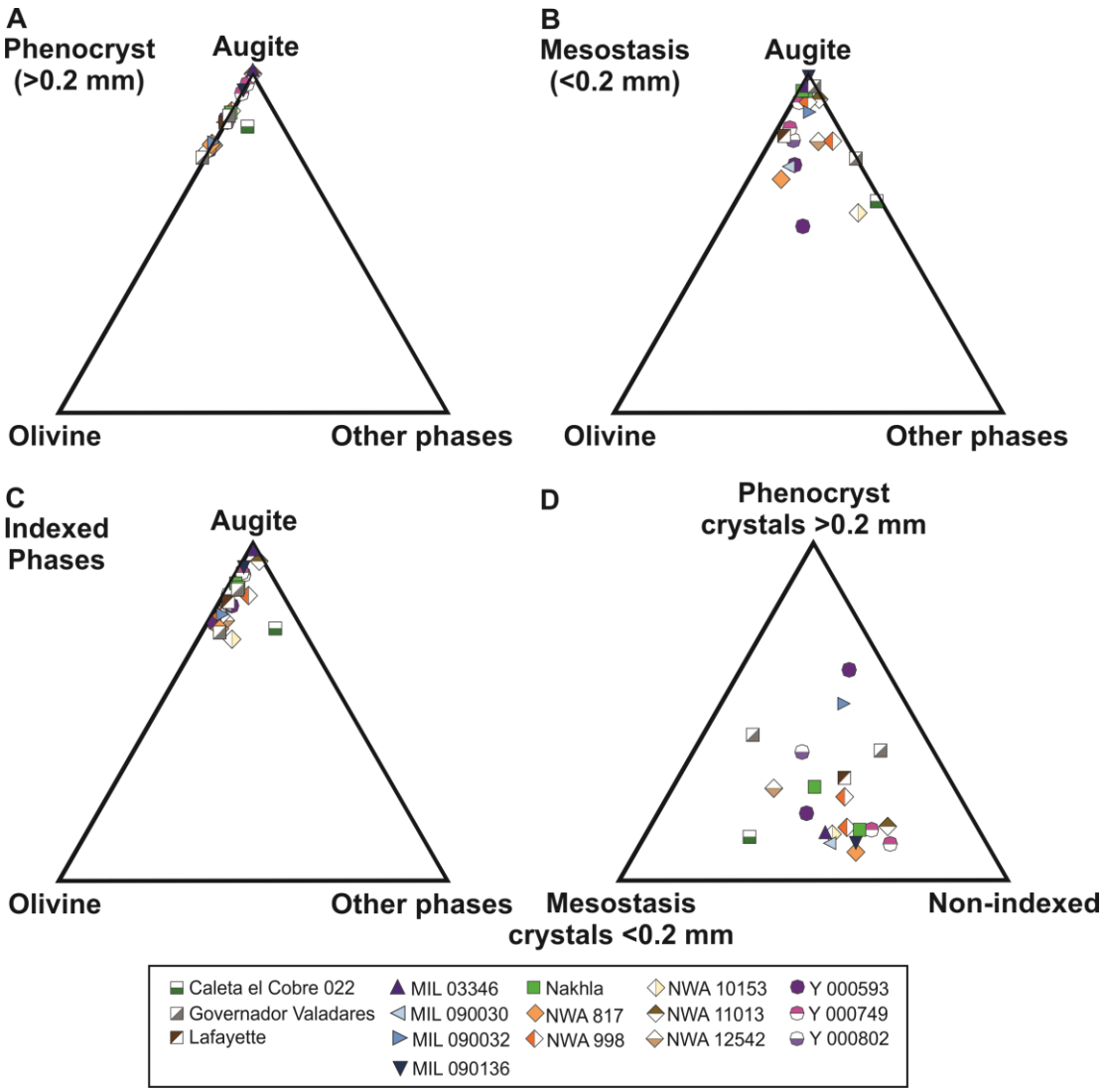

Figure 3. Compositional breakdown of EBSD datasets for analysed nakhlite samples. A) compositional breakdown of indexed phenocrysts (>0.2 mm crystals). A higher proportion of other phases is observed within Caleta el Cobre 022 reflecting the increased abundance of plagioclase within the sample. B) Compositional breakdown of indexed mesostasis (<0.2 mm crystals) C) Compositional breakdown of all indexed phases (phenocrysts and mesostasis). D) Distribution between phenocrysts crystals (>0.2 mm), mesostasis crystals (<0.2 mm), and non-indexed portions (representing the combination of voids, glass, and amorphous phases) of the large area EBSD maps. For a full breakdown of indexed phases, the reader is referred to the supplementary Table A1 and Figure A1.

3.1 Nakhlite Modal Mineralogy

Augite is observed as the dominant phase {29.2 vol% [Y 000749 (72-A)] to 66.0 vol.% [Nakhla (WAM 12965)]} in all collected datasets with variable proportions of olivine {0.3 vol.% (MIL 03346 and NWA 11013) to 14.9 vol.% [Y 000593 (127-A)]; Fig. 3}. The mineralogy is observed to be heterogeneously dispersed with pockets of increased mesostasis abundance {10 vol.% [Y 000593 (127-A)] to 60 vol.% (Caleta el Cobre 022)} relative to phenocrysts {9 vol.% NWA (817) to 62 vol.% [Y 000593 (127-A)]; Fig. 3}.

3.2 Identification of nakhlite high and low deformation regions

Assessment of combined augite and olivine mIPF major slip-system patterns for all twenty-one analysed nakhlite sections reveal nine distinct groupings (Fig. 4). These nine groups are the culmination of both high and low strain deformation within the samples. However, GROD angle maps of the sections show defined regions of high and low deformation (*e.g.*, Fig. 5). GROD maps are used to assess bending (*i.e.*, plastic deformation) within a given crystal. Here the average orientation of a crystal is chosen as a fixed reference point and the amount of deviation in orientation is depicted from blue [0 (*i.e.*, same orientation)] through to red [10° deviation (*i.e.*, the determined cutoff for a grain boundary)]. Thus, within the GROD angle map blue crystals indicate no bending within the crystal [interpreted as low strain (L)] and regions of yellowish-green through to red depict bent regions within the crystal [interpreted as high strain (H)]. In figure 5, and other analysed sections (Figs. 6–13), high strain regions are observed to form as bands. These bands are typically located in mesostasis-rich and glass-rich regions, where the associated phenocrysts often exhibit increased density of fractures, and irregular linear features that do not produce diffraction patterns higher, as well as mechanical twins (white bands).

Out of the 21 analysed sections, both NWA 10153 and NWA 11013 (Fig. 7) exhibit significantly less areas of low deformation (<2° GROD angles). In these sections the distribution of the higher deformation regions is observed to be more ubiquitous throughout the map area (Fig. 7). Section Y 000593 (127-A) on the other hand, shows minimal internal deformation relative to the other analysed sections, including its replicate section Y 000593 (106-A). Majority of the analysed crystals within the section exhibit GROD angles <1°, where the highest GROD angle observed is observed at <5° and restricted to smaller fractured crystals (Fig. 13).

Within the analysed nakhlites, augite exhibits two types of twins: simple twins (grey lines depicting 180° rotation about the {001} axis in augite) and mechanical twins (white lines representing the rotation of 180° and 60°around the {100} axis in augite and olivine, respectively). The simple twins are observed throughout the various analysed sections appearing in both low and high deformation regions (Fig. 5–13). The mechanical twins, however, only appear in high deformation regions (*e.g.*, Figs 5 and 7). The mechanical twins appear with noticeable chevron patterns within augite crystals with higher GROD angle values or crystals on the boundary of regions of increased angle misorientation, particularly within samples Caleta el Cobre 022 (Fig. 5), Governador Valadares (BM.1975,M16,P8469), Lafayette, MIL 03346, MIL 090032 (Fig. 6), NWA 817, NWA 10153, NWA 11013 (Fig. 7), NWA 12542, and Y 000593 (106-A). The mechanical twins are observed to span either the width of the crystal or where

simple twinning is also present (occurring along the {001} axis in augite) the mechanical twins form from the edge of the crystal into the simple twin boundary (light grey lines). Simple twins observed in augite appear throughout the sections appearing in both high and low deformation designated regions (Fig. 5-13).

Investigation of augite and olivine mIPF slip-system patterns for the depicted H and L regions within each analysed section (*e.g.*, Figs. 5–13), reveal shifts in the observed patterns (Figs. 14 and 15, Table 2). Overall, the dominant slip-system patterns identified in the H regions match those of the overall section slip-system patterns (Figs 13 and 14, Table 2) depicting nine different groups. However, changes in the pattern intensity and secondary slip-system patterns are observed (*e.g.*, Fig. 5). Within olivine (forsterite) mIPF plots (010)[001] combined with {hk0}(001) is observed as the most common slip-system pattern for nakhlite olivine [Group I (5 meteorites): Caleta el Cobre 022, Governador Valadares, Lafayette, NWA 12542, and Y 000593 (Fig. 4 and 13)]. Note that due to the low modal abundance of olivine within the samples overall (0.3–14.9 vol.%; Fig. 3) the number of crystals contributing to the observed crystallographic dislocations are far below those recommended for statistically relevant and whole-rock representative results (5–84 crystals, *i.e.*, <100 crystals; Watt et al., 2006) with the exception of NWA 12542 *F83-1* (136 crystals; Figs. 3–13). Overall, five unique olivine slip-system patterns [{hk0}, (010)[001], (010)[100]+(010)[001], (001)[100]/(100)[001], (010)[001]+{hk0}] are observed across the analysed samples where the overriding slip-system becomes clearly defined from the minor slip-systems with increased crystal count (Fig. 14).

For augite, 16 sections out of the 21 EBSD individual scans had statistically relevant datasets (>100 crystals; Watt et al., 2006) only 5 datasets contained <100 crystals [Governador Valadares (BM1975,M16,P8469), MIL 090032 (62; Fig. 5), NWA 817 (N8-1), NWA 998 (T1; Fig. 7), and Y 000593 (106-A); Figs. 3–5]. For augite four distinct mIPF slip-system patterns are identified with the two most commonly observed slip-system patterns involving the paring of (100)[001] (major) and (001)[100] (minor) dislocations expressed at varying proportions (groups I–III, VIII; Fig. 14). Within Figure 14, groups I and II exhibit a higher proportion of (001)[100] dislocations compared to groups III and VIII (*e.g.*, Figs. 5–7, and 12, respectively). Augite {110}[001] + {110}½<110> slip-system dislocations are also observed in groups V and VI, (010)[100]+(010)[001] slip-system dislocations in group VII (MIL 090136; Fig. 11), and a combination of multiple slip-systems, including components of (100)[001], (001)[100], {0kl}<u0w>, {110}[001] + {110}½<110>, within Y 000593 (section 127-A; Figs. 13 and 14).

When assessing the identified L regions mIPF dominant slip-system patterns were observed to shift but only for certain analysed sections [*i.e.*, sections relating to nakhlites Caleta el Cobre 022 (Fig. 5), NWA 817, NWA 11013 (Fig. 7), Nakhla, MIL 090030 (Fig. 10), MIL 090136 (Fig. 11), Y 000802 (Fig. 12), and Y 000593 (Fig. 13)].Out of the nine identified high deformation region groups, excepting group V, at least one analysed section exhibited different low deformation region mIPF slip-system patterns (Table 2, Figs. 14 and 15). For the sections that showed different slip-system patterns between the H and L regions, pattern shifts were often only observed to occur in either olivine and augite, where olivine is the more likely mineral to exhibit a shift (Fig, 15, Table 2). However, additional shifts in mIPF slip-system patterns and intensity can also be observed as additional slip-systems patterns within the L region mIPFs even when the major slip-system pattern remains the same (Fig. 15). All L region mIPF slip-system patterns appear unique to the individual meteorite. More importantly, different low deformation

mIPF slip-system patterns are observed to occur within group II (Table 2, Fig. 15), where meteorites MIL 03346 and NWA 817 exhibit the same H region mIPF slip-system patterns but distinct L region mIPF patterns (Figs. 14 and 15, Table 2). This indicates that the cause of the H region mIPF slip-system patterns most likely independent of the L region mIPF slip-system patterns.

In order to assess consistency in the presented analysis replicate sections were run for five of the sixteen analysed nakhlites. In these replicate sections, the same major augite and olivine mIPF slip-system patterns (both H and L region) are expressed for the meteorites Governador Valadares, NWA 998, and Y 000749. However, discrepancies in olivine slip-system patterns are observed between the two Nakhla sections {USNM 426-1 exhibiting (010)[001] H region patterns and WAM 12965 exhibiting (001)[100]/(100)[001] H region patterns} as well as differences in both augite and olivine slip-system patterns between the two Y 000593 sections {106-A exhibiting dominant (100)[001] with minor (001)[100] for augite and (010)[001] with {hk0}[001] for olivine and section 127-A exhibiting multiple dislocations in augite and (010)[100]+(010)[001] for olivine}. Furthermore, low amounts of internal misorientation are observed within the GROD angle map (Fig. 13). 120° triple junctions (typical annealing textures) are also observed within Y 000593 (127-A)'s clustered olivine within which were not identified within Y 000593 (106-A). The observed variability of slip-system patterns within Nakhla and Y 000593 meteorites have direct implications for methodological parameters *e.g.*, step-size and number of assessed crystals, textural heterogeneity, *etc.* which will be further evaluated in the discussion.

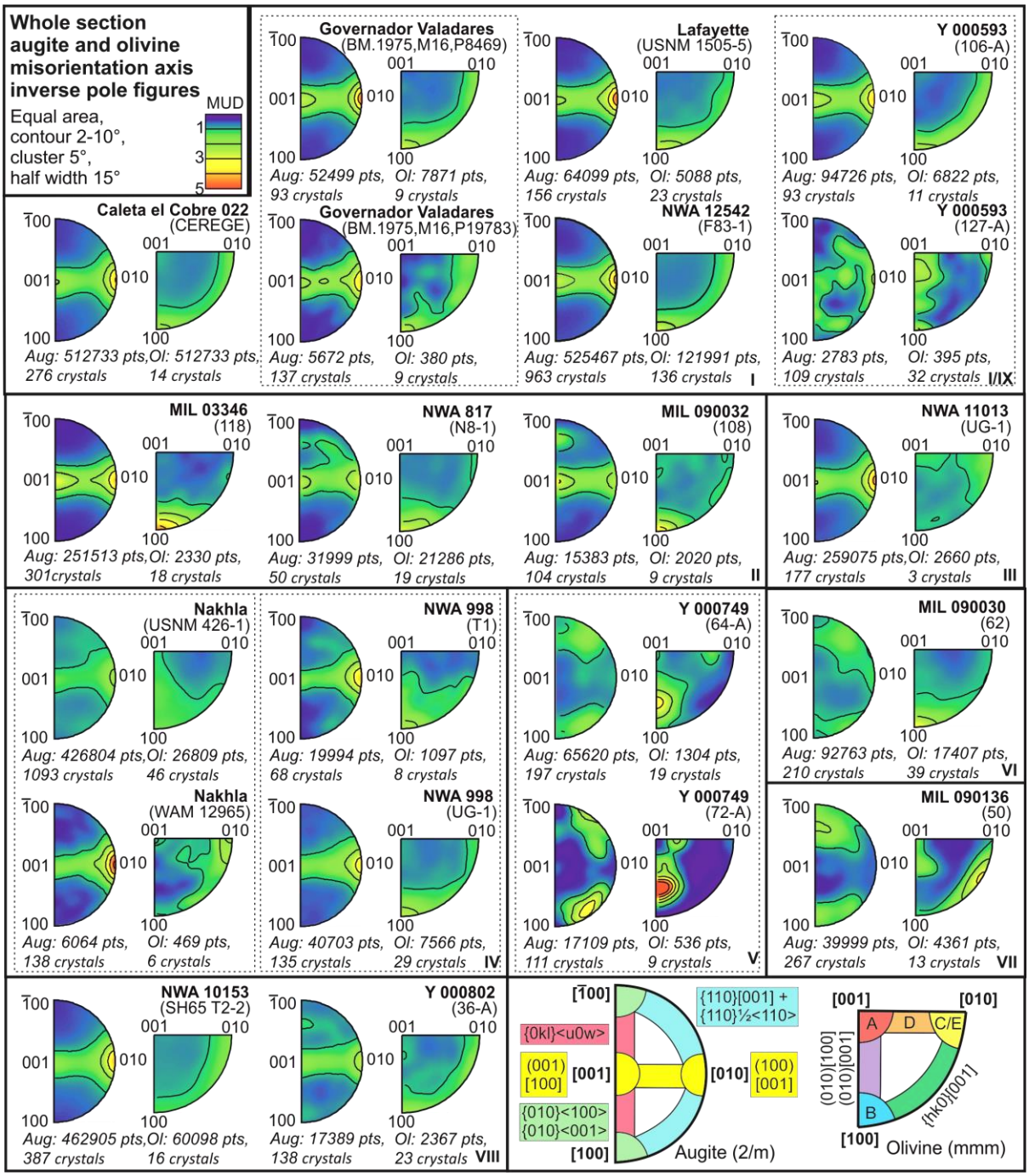

Figure 4. Misorientation axis inverse pole figure plots (mIPF) for nakhlite whole section data. Augite (half-circles) and olivine (quarter circles) represented as their fundamental sectors (lowest form of crystal symmetry) where the misorientation is referenced against the crystal co-ordinate system. We identify 8 (potentially 9) different major slip system combinations for the nakhlites based on their respective keys (bottom right box) where each colour indicates a different type of dominant slip-system. Olivine key: A = (010)[100], B = (010)[001], C = (100)[001], D = {0kl}[100], E = (001)[100].

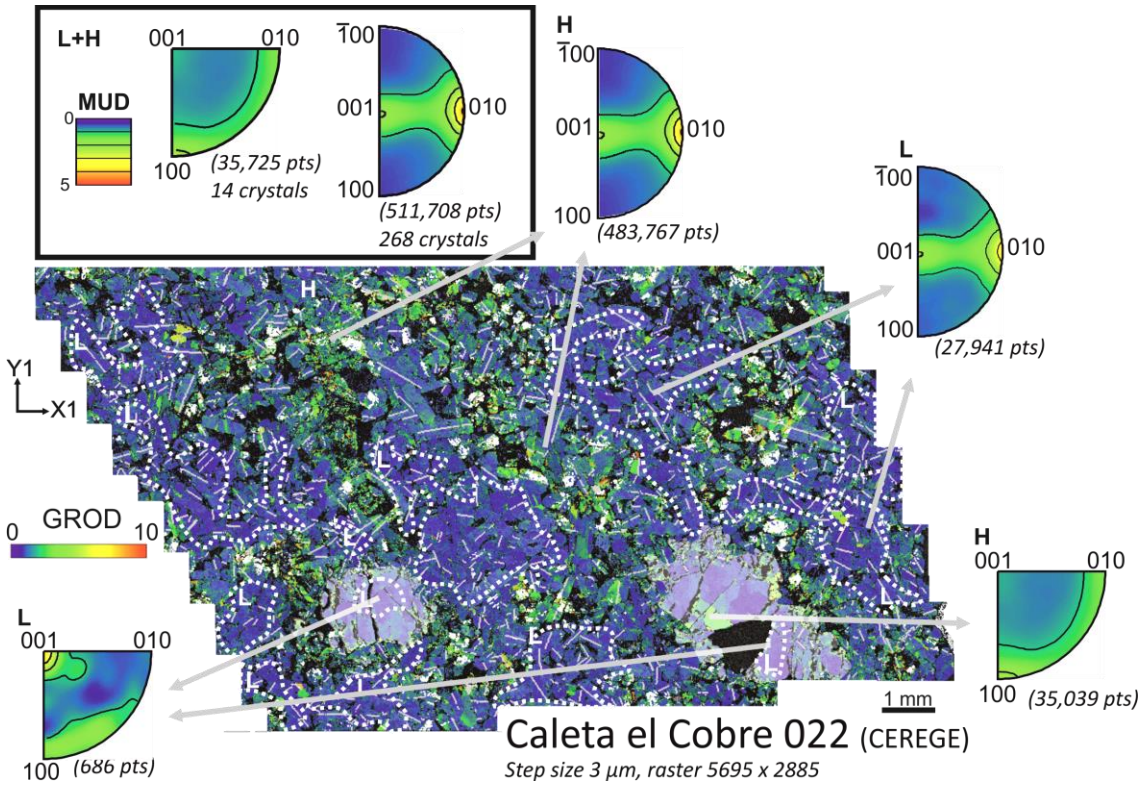

Figure 5. Grain relative orientation (GROD) angle map (0–10°) Caleta el Cobre 022 (group I) with augite and olivine misorientation axis inverse pole figures (mIPF)s for low deformation regions (L), high deformation regions (H), and whole section representative slip-system signatures (L+H). Combined slip-system signature is dominated by high deformation signature. Between L and H mIPFs, a shift is observed in olivine signature while augite signatures remain constant. The GROD map depicts the changes in crystallographic orientation within a given crystal between 0–10° relative to the average crystallographic orientation of the crystal. Higher internal misorientations 3–10° angles are observed as green-red regions in each section. These bands of higher internal misorientation align with regions of increased mesostasis abundance. Augite and olivine mechanical twins [white lines; {100} axis in augite (180° rotation) and olivine (60° rotation)], and regions of higher fracture density. Augite simple twins (light grey lines, 180° rotation about {001} axis) an indicator of shock deformation appear throughout both the high and lower misorientation regions. Olivine within the sample is indicated by the white transparent layer.

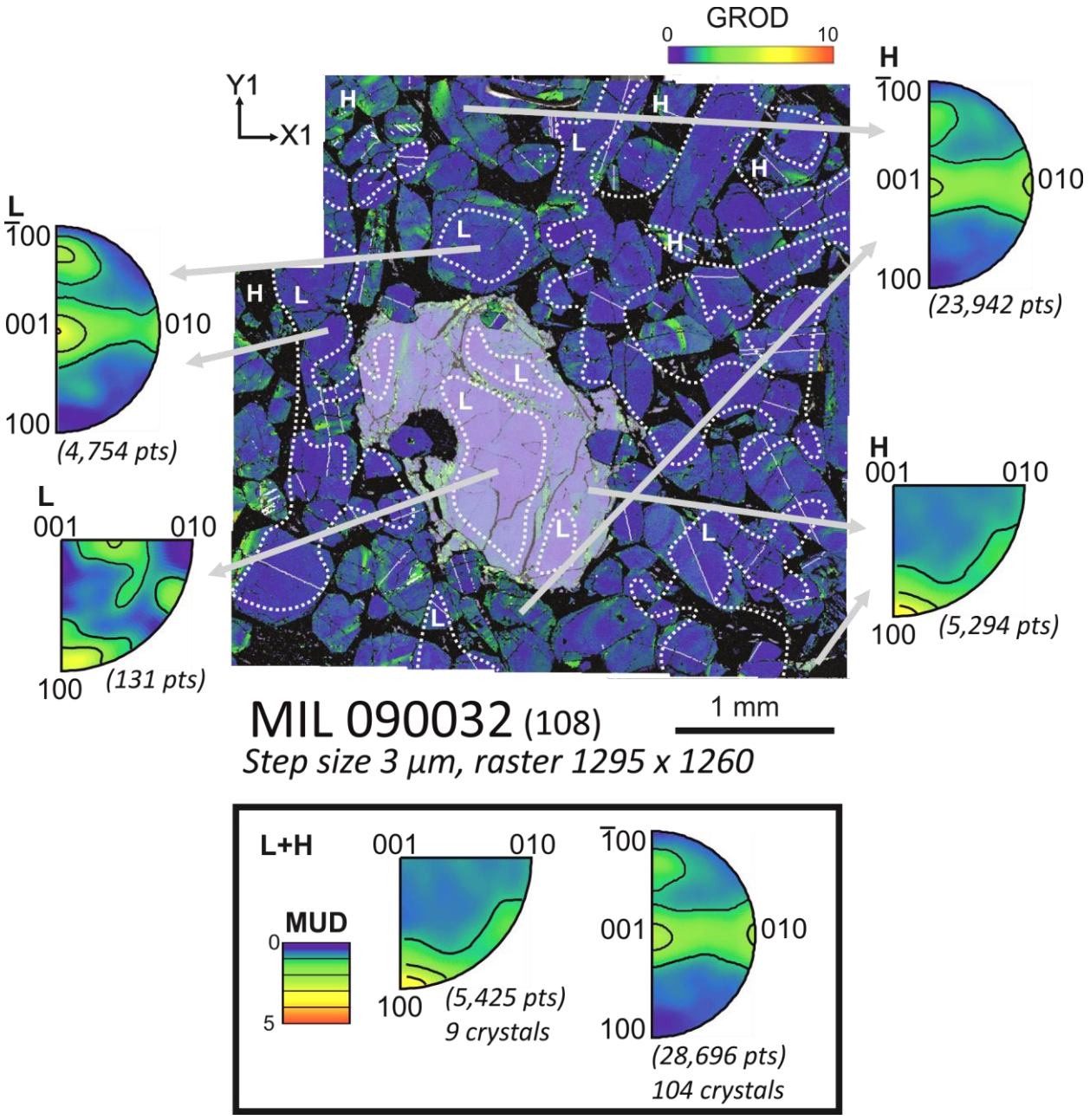

Figure 6. GROD angle map (0–10°) of MIL 090032 (group II with augite and olivine mIPFs for low deformation regions (L), high deformation regions (H), and whole section representative slip-system signatures (L+H). From the mIPF plots signatures from the high deformation regions (H) are seen to dominate the whole section signature. Between L and H mIPFs a subtle shift in signature is observed within augite and a significant shift is observed in olivine. In the GROD angle map bands of higher internal misorientation align with regions of increased mesostasis abundance. Augite and olivine mechanical twins [white lines; {100} axis in augite (180° rotation) and olivine (60° rotation)], and regions of higher fracture density. Augite simple twins (light grey lines, 180° rotation about {001} axis) an indicator of shock deformation appear throughout both the high and lower misorientation regions. Olivine within the sample is indicated by the white transparent layer.

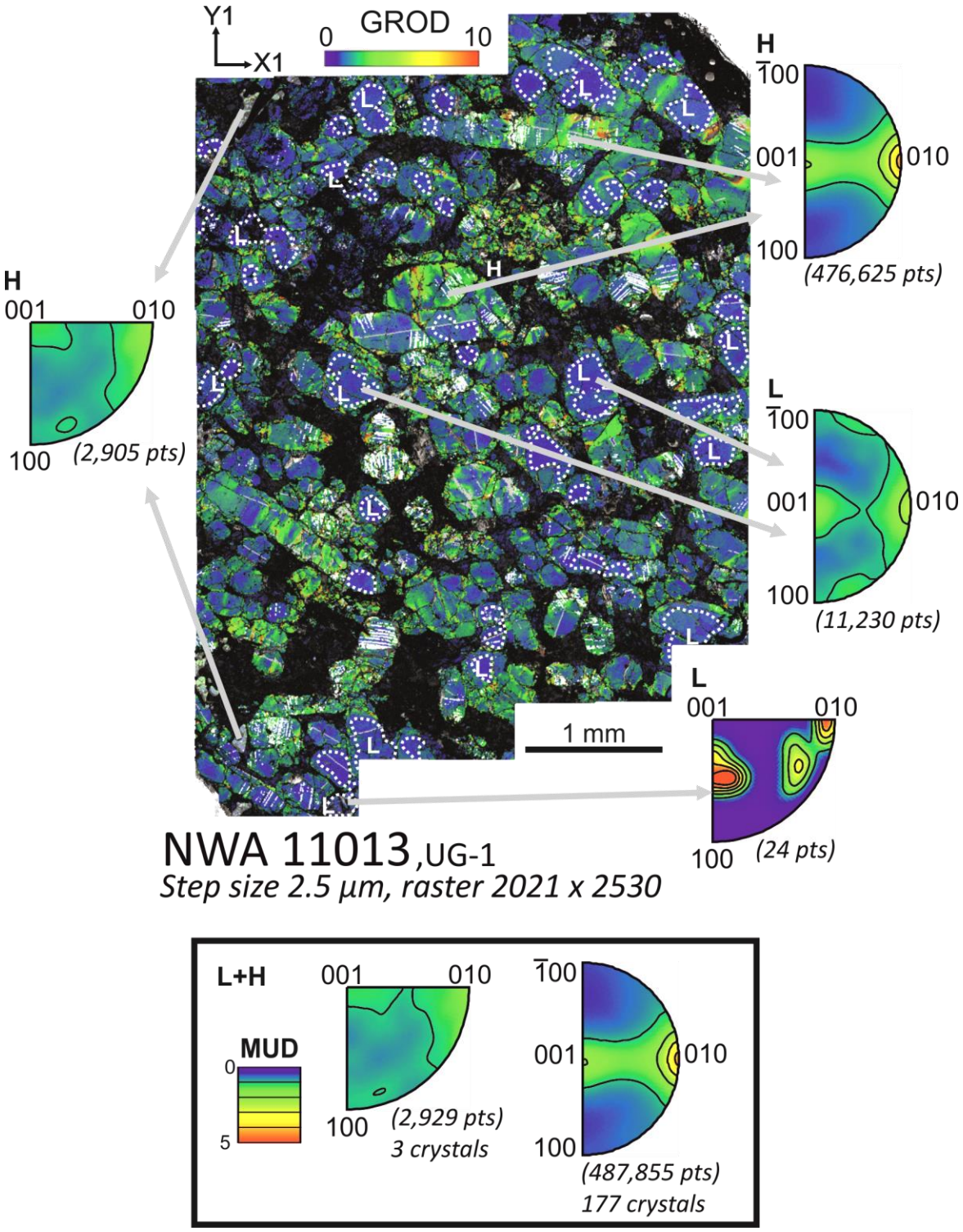

Figure 7. GROD angle map (0–10°) of NWA 11013 (group III) with augite and olivine mIPFs for low deformation regions (L), high deformation regions (H), and whole section representative slip-system signatures (L+H). Whole section signatures are dominated by H signatures. A region signatures show a combination of L region as well as potential low strain slip-systems. In the GROD angle map bands of higher internal misorientation align with regions of increased mesostasis abundance. Augite and olivine mechanical twins [white lines; {100} axis in augite

(180° rotation) and olivine (60° rotation)], and regions of higher fracture density. Augite simple twins (light grey lines, 180° rotation about {001} axis) an indicator of shock deformation appear throughout both the high and lower misorientation regions. Olivine within the sample is indicated by the white transparent layer.

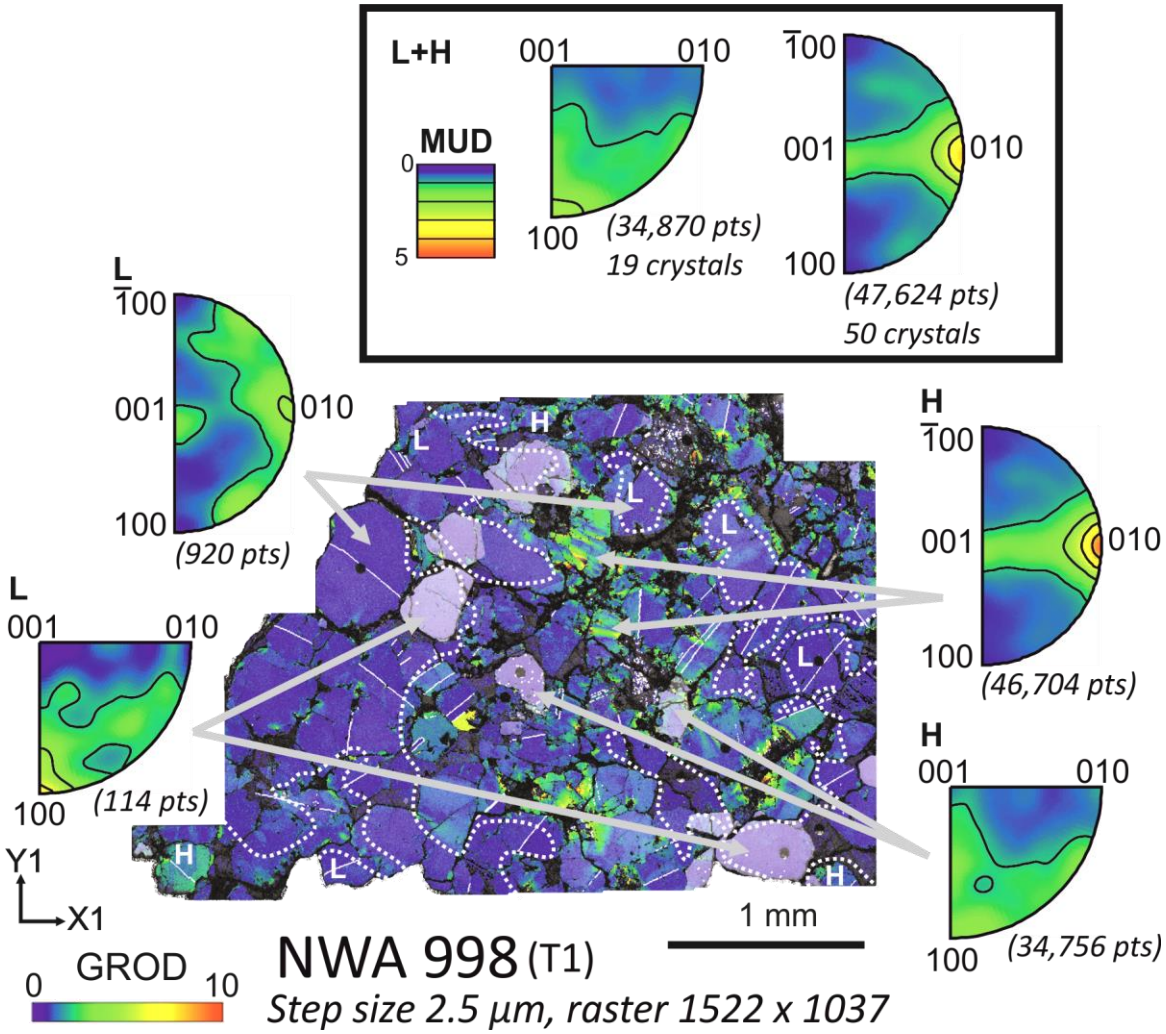

Figure 8. GROD angle map (0–10°) of NWA 998 (T1; group IV with augite and olivine mIPFs for low deformation regions (L), high deformation regions (H), and whole section representative slip-system signatures (L+H). No shift is observed between olivine L and H region signatures while augite shows a shift in slip-system pattern dominance between the L and H regions. In the GROD angle map bands of higher internal misorientation align with regions of increased mesostasis abundance. Augite and olivine mechanical twins [white lines; {100} axis in augite (180° rotation) and olivine (60° rotation)], and regions of higher fracture density. Augite simple twins (light grey lines, 180° rotation about {001} axis) an indicator of shock deformation appear throughout both the high and lower misorientation regions. Olivine within the sample is indicated by the white transparent layer.

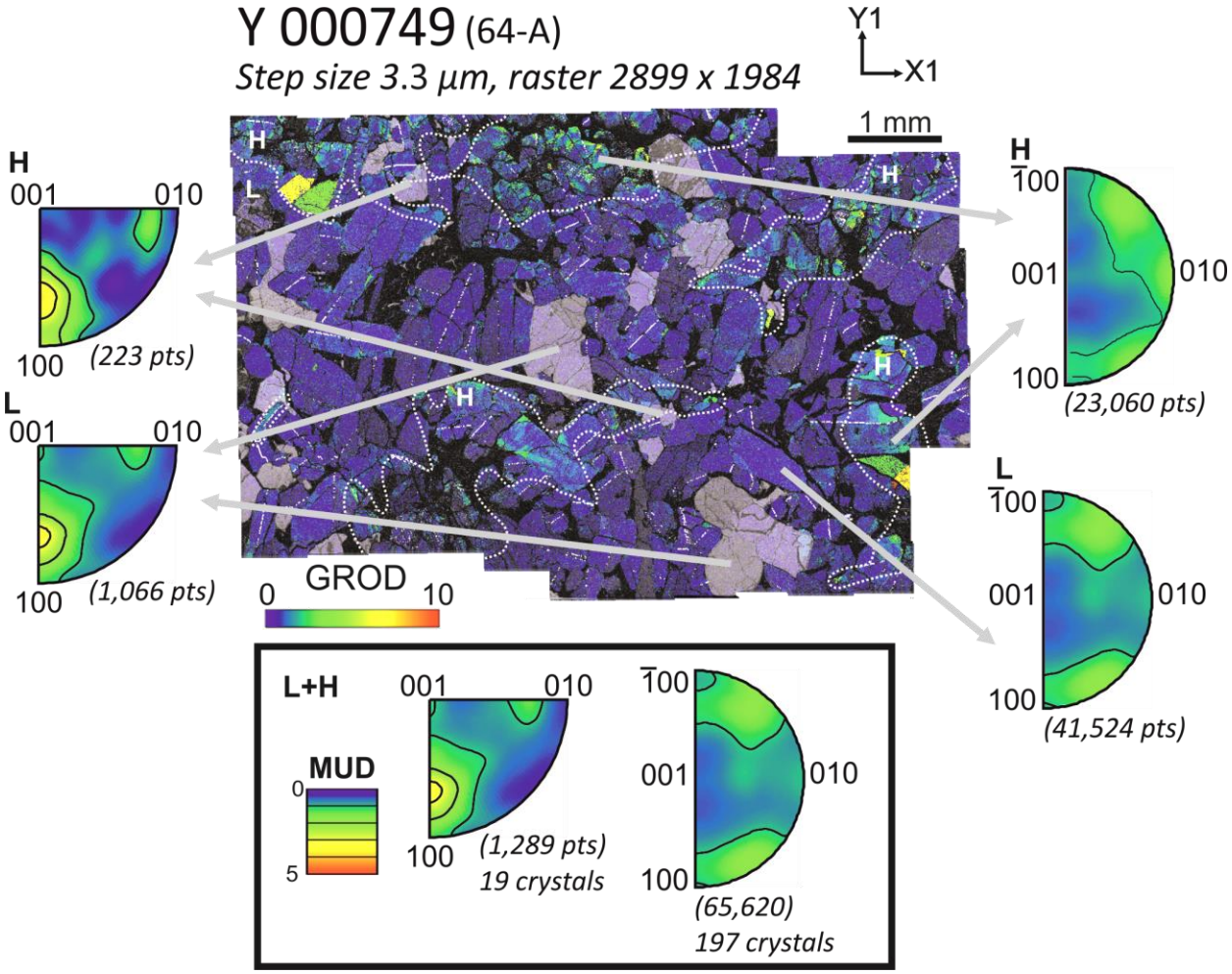

Figure 9. GROD angle map (0–10°) of Y 000749 (64-A; group V) with augite and olivine mIPFs for low deformation regions (L), high deformation regions (H), and whole section representative slip-system signatures (L+H). No difference is observed between L and H region slip-system patterns. In the GROD angle map bands of higher internal misorientation align with regions of increased mesostasis abundance. Augite and olivine mechanical twins [white lines; {100} axis in augite (180° rotation) and olivine (60° rotation)], and regions of higher fracture density. Augite simple twins (light grey lines, 180° rotation about {001} axis) an indicator of shock deformation appear throughout both the high and lower misorientation regions. Olivine within the sample is indicated by the white transparent layer.

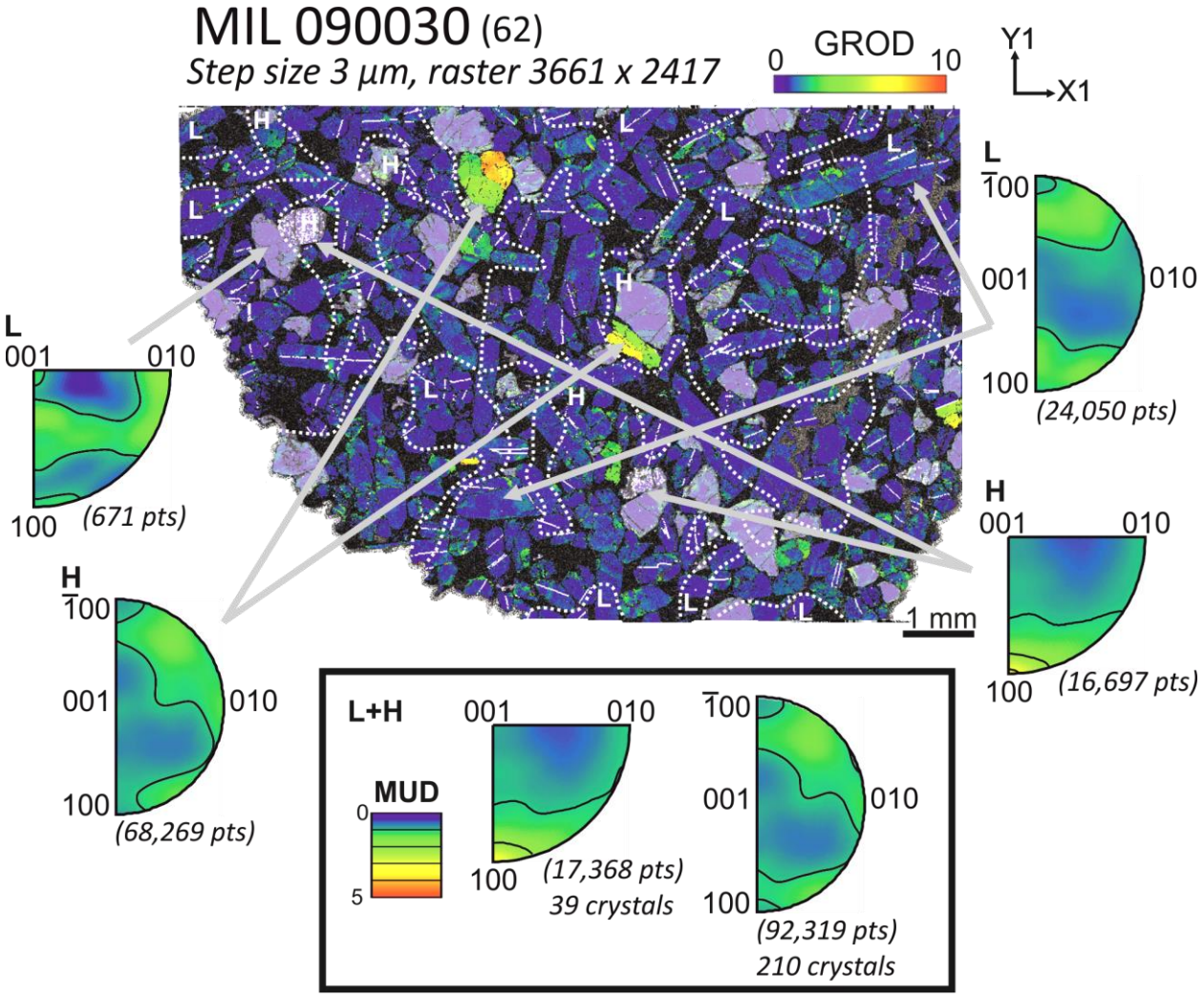

Figure 10. GROD angle map (0–10°) of MIL 090030 (group VI) with augite and olivine mIPFs for low deformation regions (L), high deformation regions (H), and whole section representative slip-system signatures (L+H). H region patterns dominate the whole system patterns. A shift in slip-system pattern is observed between the low and high deformation regions for both augite and olivine. In the GROD angle map bands of higher internal misorientation align with regions of increased mesostasis abundance. Augite and olivine mechanical twins [white lines; {100} axis in augite (180° rotation) and olivine (60° rotation)], and regions of higher fracture density. Augite simple twins (light grey lines, 180° rotation about {001} axis) an indicator of shock deformation appear throughout both the high and lower misorientation regions. Olivine within the sample is indicated by the white transparent layer.

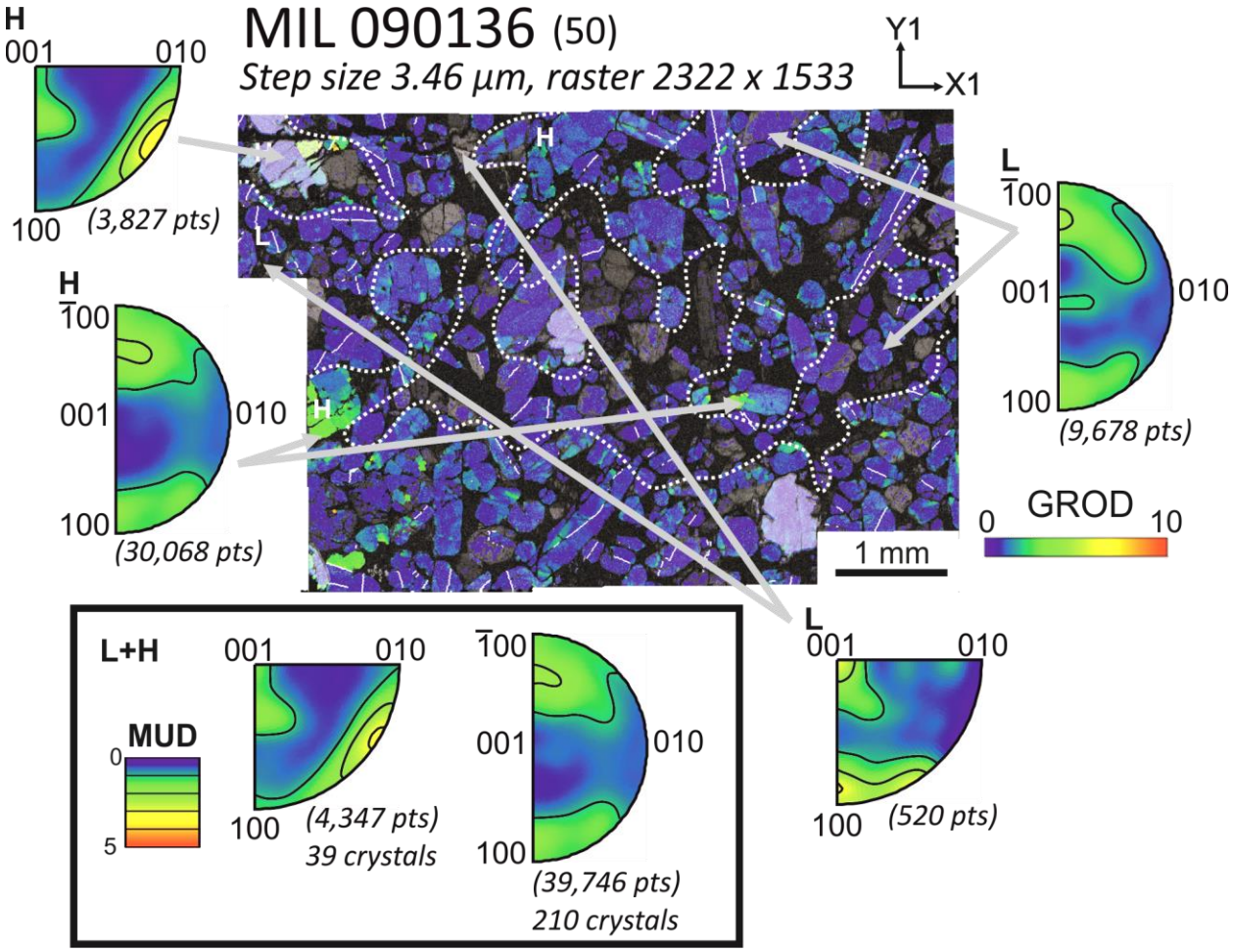

Figure 11. GROD angle map (0–10°) of MIL 0901362 (group VII) with augite and olivine mIPFs for low deformation regions (L), high deformation regions (H), and whole section representative slip-system signatures (L+H). A slight shift in slip-system pattern is observed within olivine between high and low deformation regions with little change observed in augite. Overall slip-system patterns from the high deformation regions are observed to dominate the expressed slip-system patterns for the overall scan. In the GROD angle map bands of higher internal misorientation align with regions of increased mesostasis abundance. Augite and olivine mechanical twins [white lines; {100} axis in augite (180° rotation) and olivine (60° rotation)], and regions of higher fracture density. Augite simple twins (light grey lines, 180° rotation about {001} axis) an indicator of shock deformation appear throughout both the high and lower misorientation regions. Olivine within the sample is indicated by the white transparent layer.

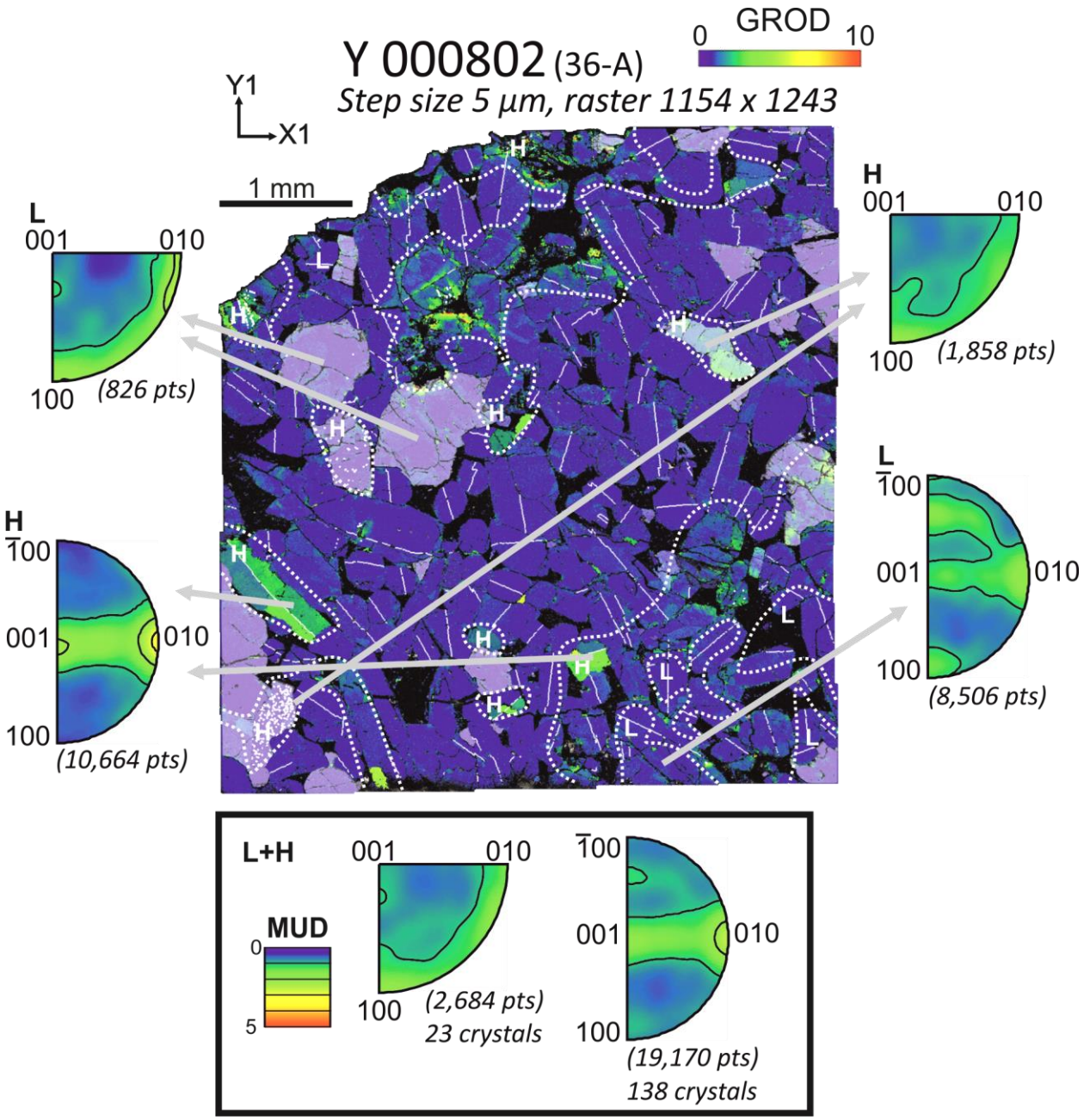

Figure 12. GROD angle map (0–10°) of Y 000802 (group VIII) with augite and olivine mIPFs for low deformation regions (L), high deformation regions (H), and whole section representative slip-system signatures (L+H). Whole scan slip-system patterns show a high influence from the high deformation regions with some contribution from the low deformation regions. For the low deformation slip-system patterns, additional patterns are observed within the low deformation augite as well as olivine indicating potential mantle deformation in combination with shock. In the GROD angle map bands of higher internal misorientation align with regions of increased mesostasis abundance. Augite and olivine mechanical twins [white lines; {100} axis in augite (180° rotation) and olivine (60° rotation)], and regions of higher fracture density. Augite simple twins (light grey lines, 180° rotation about {001} axis) an indicator of shock deformation appear

474 throughout both the high and lower misorientation regions. Olivine within the sample is
475 indicated by the white transparent layer.

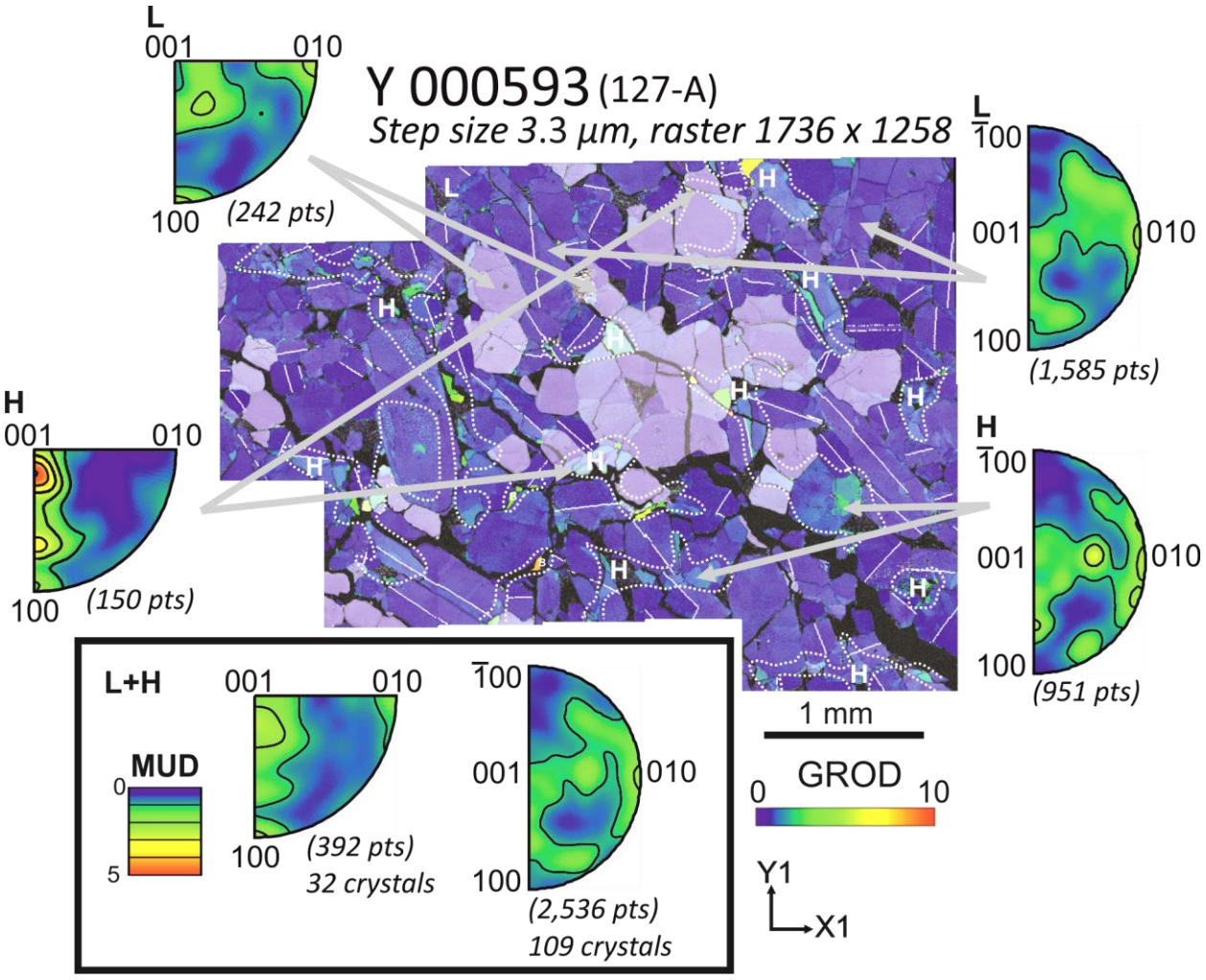

476
477 **Figure 13.** GROD angle map (0–10°) of Y 000593 (group IX) with augite and olivine mIPFs for
478 low deformation regions (L), high deformation regions (H), and whole section representative
479 slip-system signatures (L+H). A shift in slip-system pattern is observed between the high and
480 lower deformation olivine which are both expressed in the whole scan slip-system pattern. No
481 change is observed in the augite slip-system patterns. In the GROD angle map bands of higher
482 internal misorientation align with regions of increased mesostasis abundance. Augite and olivine
483 mechanical twins [white lines; {100} axis in augite (180° rotation) and olivine (60° rotation)],
484 and regions of higher fracture density. Augite simple twins (light grey lines, 180° rotation about
485 {001} axis) an indicator of shock deformation appear throughout both the high and lower
486 misorientation regions. Olivine within the sample is indicated by the white transparent layer.

487

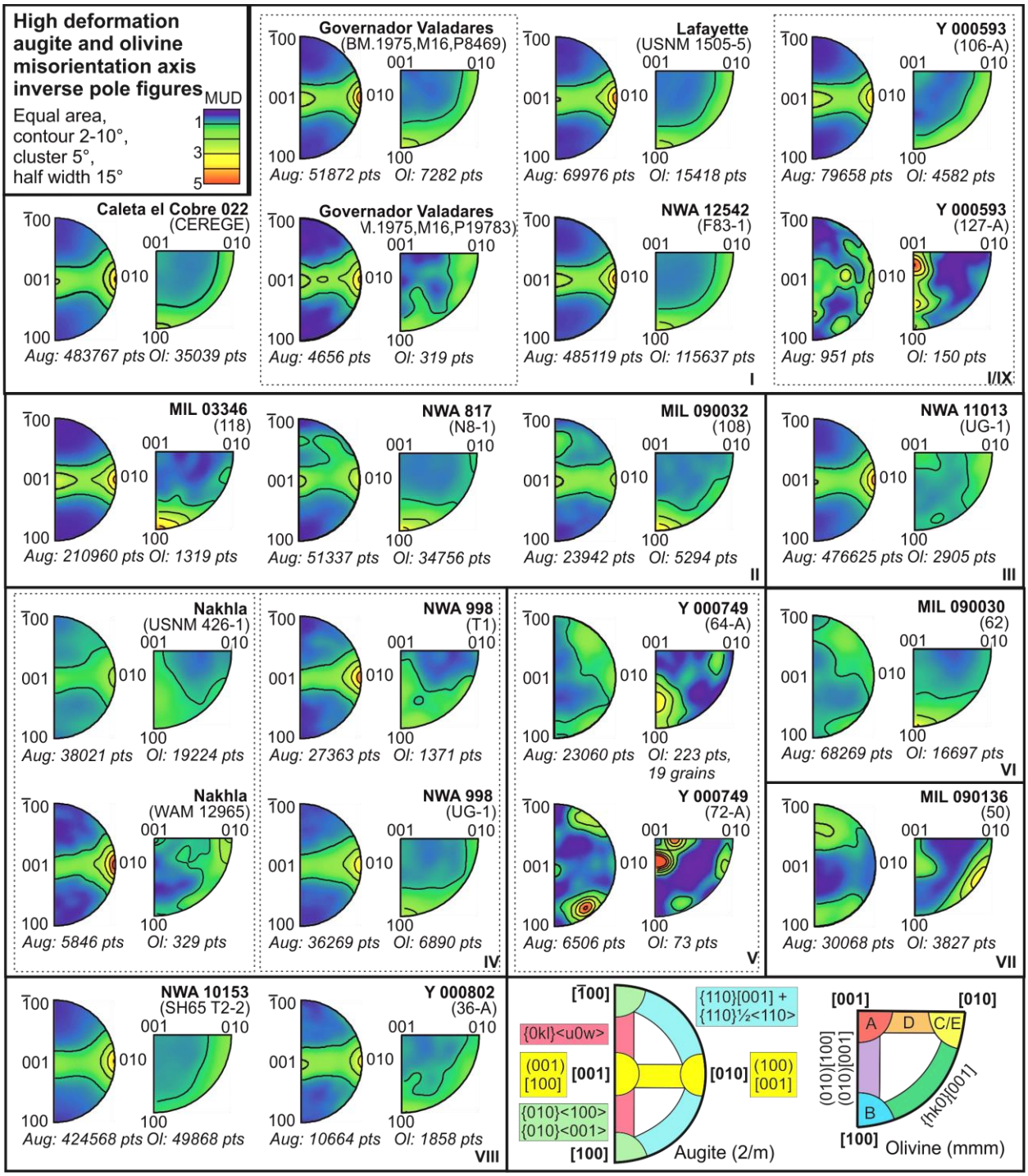

Figure 14. High strain deformation mIPF plots for augite and olivine. Nine different major slip system combinations are identified for the nakhlites that match whole section mIPF patterns. Slip-system patterns are based on the respective keys (bottom right box) where each colour indicates a different type of dominant slip-system. Olivine key: A = (010)[100], B = (010)[001], C = (100)[001], D = {0kl}[100], E = (001)[100].

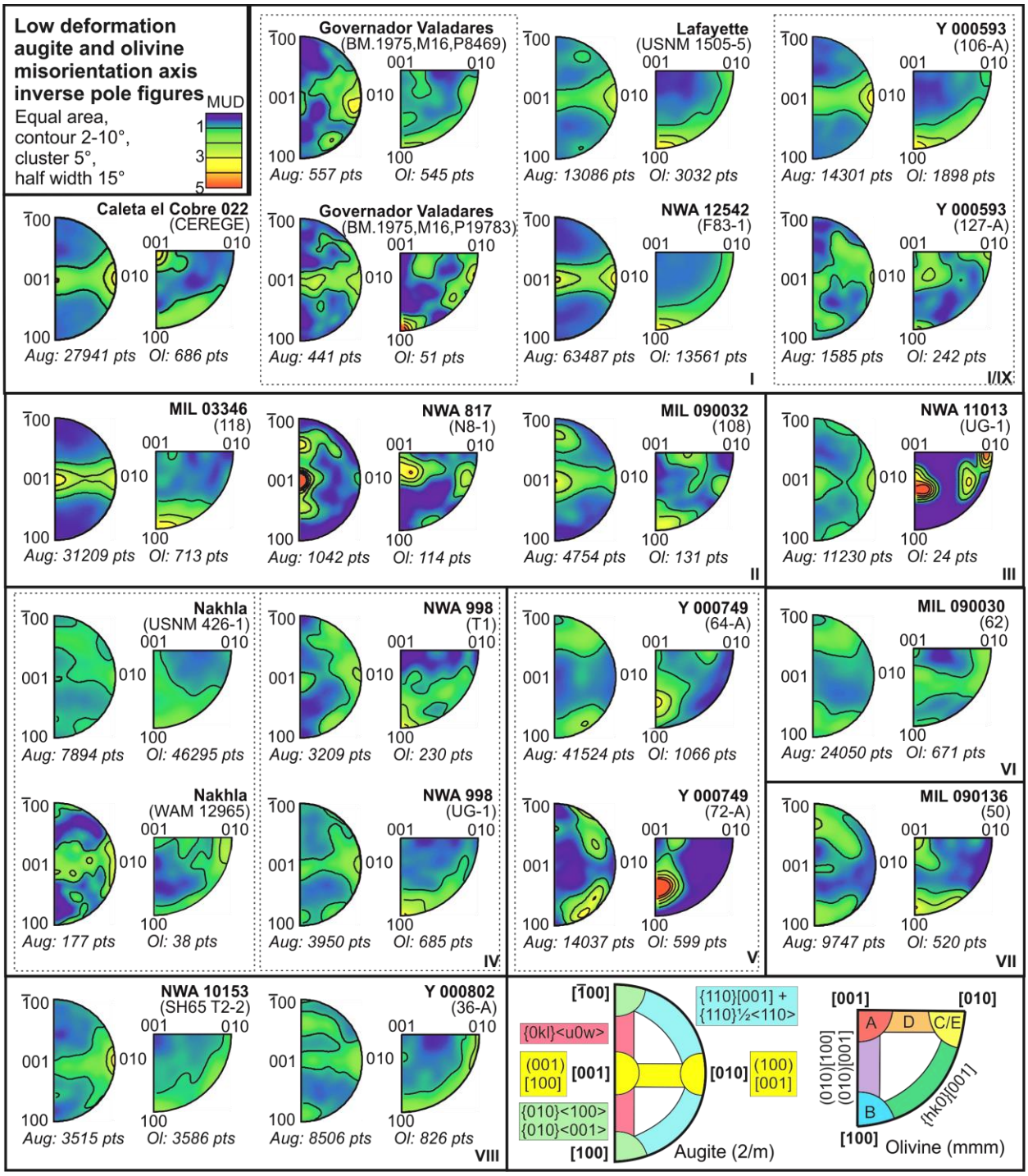

Figure 15. Low strain deformation mIPF plots for augite and olivine. Variation from high strain deformation slip-system patterns are observed for 9 of the 21 analysed sections. Two different low strain mIPF slip-system patterns are observed within group II, while no significant shift in pattern is observed for group V. Slip-system patterns are based on the respective keys (bottom right box) where each colour indicates a different type of dominant slip-system. Olivine key: A = (010)[100], B = (010)[001], C = (100)[001], D = {0kl}[100], E = (001)[100].

4 Discussion

4.1 Large area electron backscatter diffraction mapping (EBSD) appropriate step-size for slip-system pattern determination

Large area mapping for EBSD is becoming a more common tool for observing textural fabrics such as CPO within samples. The ability to analyse whole thin/thick sections however, is still a time-consuming and data intensive process - and is not without associated error (*e.g.*, mis-indexing, improper-indexing, beam drift *etc.*) even with recent technological advancements (Winiarski et al., 2021). The ability to cover larger areas is often counteracted by using larger step sizes, where the limiting factor for step size is controlled by the size of the crystal (to ensure >10 pixels/EBSD measurements are acquired per crystallite to adequately define its orientations), sacrificing higher resolution (≤4 μm step size) required for microstructural analysis (Ruggles & Fullwood, 2013). Whilst microstructurally focused EBSD studies that utilise a smaller step size ≤4 μm will often observe either multiple single crystals from specific regions of a section or a selection of small areas where the total crystal count is below statistically stable results (<100–150 crystals; Vollmer, 1990; Skemer et al., 2005). Within the nakhlite datasets, five sections with a step size >4 μm (ranging from 4.5–15 μm) were run (Table 1), where three of these sections had a replicate section which was run at a step size <4 μm (Table 1). Replicate sections for two samples were also run at higher resolution (*i.e.,* step size <4 μm). Comparing these replicate sections run at different step sizes clearer dominant slip-system patterns are able to be discerned from ≤4 μm particularly with smaller area maps. However, data presented here suggests that confirmation of similar slip-system patterns across multiple sections could be achieved using larger step sizes >4 μm on the condition that at least one of the sections is run at ≤4 μm.

4.1.1 Analytical limitations and essential criteria for slip-system determination in large area EBSD datasets

Comparing results between replicate datasets, little difference is observed in the GROD angle distribution patterns between each section. However, the lower resolution in some of the datasets makes it more difficult to accurately assess the variability in GROD angle across a given crystal *i.e.,* larger GROD angles are observed where most of the crystal is at a single value (*e.g.,* Fig. 8). The lower resolution of specific datasets also makes it difficult to ascertain the presence and interaction between a given crystal and any mechanical twinning present (Fig. 5). Comparing mIPF plots for the replicate sections, the number of crystals analysed is observed to have a greater impact on the determination, refinement, and identification of the samples dominant active slip-system over the specific step size of the analysis (Figs. 4, 14, and 15), with the caveat that the chosen step size is appropriate for the identification of slip-systems *i.e.,* ≤4 μm. Note that this observation is only relevant when assessing the overriding major dislocation slip-system expressed within a section. In order to investigate microstructural changes between different regions throughout the sample, assess the higher and lower deformation regions within the nakhlite samples (Figs. 5–13, Table 2), inspect secondary slip-systems contributing to a given sample, or investigate how sub-crystal boundary interactions in combination with crystal orientation contribute to the overall observed deformation then a higher resolution step size ≤4 μm is required.

542 *4.1.2 Is large area EBSD derived slip-systems whole rock representative?*

543 Analysis of the replicate sections revealed consistent augite and olivine slip system
544 patterns for whole section, high deformation and low deformation datasets within Governador
545 Valadares, NWA 998, and Y 000749 (Figs. 14 and 15, Table 2). However, the same correlation
546 is not observed within the replicate Nakhla or Y 000593 sections (Figs. 14 and 15, Table 2). For
547 the two Nakhla replicate sections there is consistency in the slip-system patterns of augite for all
548 three datasets (whole section high deformation, and low deformation) and a discrepancy in
549 expression of slip-system patterns in olivine where the types of slips are present in both but the
550 dominantly expressed slip-system is different for whole section and high deformation datasets.
551 The difference in expressed olivine slip-system patterns could be a function of the crystal
552 differential (40 crystals and 26,340 datapoints) between the two datasets, the modal distribution
553 of crystals between the sections, the larger (15 µm) step size of section WAM 12965 compared
554 to USNM 426-1 (3 µm; Table 1), or the heterogeneous influence and distribution of shock
555 between the two sections in relation to olivine's location. More consistent MUD patterns are
556 observed for augite within section USNM 426-1 (MUD = 0.53–1.37) compared to section WAM
557 12965 (MUD = 0.35–2.48) despite both datasets containing statistically relevant amounts of
558 crystals, unlike the olivine mIPF plots (Fig. 13). A similar fluctuation in MUD values is also
559 observed between the two replicate Governador Valadares sections. In this instance, consistent
560 slip-system patterns for all three datasets are observed, where each of the large area EBSD maps
561 sample equivalent areas olivine (9 crystals each) and augite crystals (93 vs. 137 crystals; Fig. 4,
562 Table 2). The only difference being a similar analysis step size discrepancy between the two
563 Governador Valadares replicate sections as Nakhla (Table 1). For both NWA 998 replicate
564 sections which have a 0.5 µm step size differential and Y 000749 replicate sections which have
565 the same analysis step size no fluctuations are observed in the dominant augite and olivine slip-
566 system patterns Across the nakhlite datasets statistically relevant crystal sets at <4 µm step size
567 were observed to have cleaner MUD distribution patterns and narrower MUD ranges [*e.g.*,
568 Governador Valadares MUD = 0.35–4.55 vs 0.25–3.56 (augite mIPF) and MUD = 0.55–2.72 vs.
569 0.35–2.68 (olivine mPF) for sections BM.1975,M16,P8469 and BM.1975,M16,P19783,
570 respectively; Fig. 4, 14 and 15, Table 1]. Where decreased crystal count and larger step sizes
571 contribute to increased MUD distributions within the mIPF plots [*e.g.*, Nakhla MUD = 0.63–2.30
572 vs 0.27–5.26 (augite mIPF) and 0.53–1.37 vs. 0.34–2.48 (olivine mIPF) for sections USNM 426-
573 1 and WAM 12965, respectively; Figs. 4, 14, and 15; Table 2]. Suggesting that differences
574 observed within Nakhla's replicate section olivine slip-system patterns is most likely to be the
575 result of both analysis step size and analysis area.

576 Out of all the replicate sections, only the Y 000593 sections exhibited completely
577 different augite mIPF slip-system patterns {(100)[001]:(001)[100] and multiple slip-systems for
578 sections 106-A and 127-A, respectively} and olivine mIPF slip-system patterns {(010)[001] with
579 {hk0}[001] and (010)[100]+(010)[001] for sections 106-A and 127-A, respectively} which in a
580 low strain mantle system would indicate low temperature moderate strain conditions for section
581 106-A and high temperature low strain condition for section 127-A (Figs 12–15). Even when
582 assessing the low deformation regions only the slip-system patterns for both olivine and augite
583 express wildly different extrinsic parameter conditions (Fig. 12, Table 2). mIPF patterns for
584 section 127-A indicate multiple slip-systems and augite and olivine (010)[100]+(010)[001] slip-
585 systems which cluster towards (010)[100] slip (Fig. 12). The combination of slip-system patterns
586 within both augite and olivine suggests deformation within section 127-A to have occurred under

high temperature conditions (Figs. 14 and 15). Multiple slip-systems observed within the augite mIPF have been associated with partial melting and recrystallisation conditions (Fig. 15; Ave Lallemant, 1978). Suggested higher temperature conditions from mIPF slip-system patterns would be consistent with observed olivine annealing textures [120° triple junctions in clustered olivine within Y 000593 (127-A); Fig 12] and lower dispersed deformation (GROD angle values), which are not observed within Y 000593 (106-A). For section 106-A clear banding of high deformation can be observed within the GROD angle map, where slip-system patterns even within the low deformation regions still express high deformation region signatures (Table 2). Deformation, particularly that associated with shock metamorphism, is known to be heterogeneous (Stöffler et al., 2018). Variability in temperature and pressure resulting from hypervelocity impacts can create pockets within a sample that may have experienced higher temperature and/or pressure conditions. Furthermore, recrystallisation has been shown to override a given crystal's deformation history to its new recrystallised conditions (Muto et al., 2011; Wenk & Tomé, 1999; Yao et al., 2019). Annealing on the other hand has been shown to significantly reduce, overprint, and sometimes completely override a given crystal's former deformation history to the current conditions acting on the sample during the annealing process (Farla et al., 2011; H. Jung et al., 2006). Investigations of shock deformation within the Yamato nakhlites has shown some of the lowest bulk shock pressures (5–14 GPa for Y 000593) within the already low shocked nakhlites (Fritz, Artemieva, et al., 2005). However, the presence of annealing within the sample could have contributed to the lower inferred shock pressure values. Thus, the differences in slip-system patterns observed between the two Y 000593 sections could therefore indicate either an extreme change in emplacement environment, which would have had to occur within the mm scale of the meteorite stone (Imae et al., 2005), shock banding within the meteorite, or could indicate that the two sections represent two distinct neighbouring geological units present within the same meteorite stone.

4.1.3 Large area EBSD derived slip-systems for extrinsic parameter determination

Studies on assessing crystallographic slip-systems at a statistically relevant scale are still in their infancy. This is predominantly due to the specific cost, time, and equipment constraints (*e.g.,* beam stability, indexing time, computer processing ability, post processing time *etc.*) required to run ≤4 μm step size large area EBSD experiments. Comparison between collected EBSD datasets show that in order to use crystallographic slip-systems to assess extrinsic parameters within a given sample, higher resolution (step sizes ≤4 μm) large area EBSD is required to ensure reasonable and rational results (Figs. 4, 14, and 15). Rocks in general are not homogeneous, while rocks that have experienced shock metamorphism (which in the case of MIL 03346, Lafayette, and most likely the entire nakhlite suite occurred on at least two occasions; Daly et al., 2019) exhibit even higher levels of microstructural and mineralogical heterogeneity (*e.g.*, Figs. 5–13), through increased fracturing, partial melting, and partial recrystallisation (Stöffler et al., 2018). Experimental data has shown that a crystal's orientation relative to external deformation parameters is one of many important factors for the selection and activation of particular slip-systems (Bascou et al., 2002; Bernard et al., 2019; Kollé & Blacic, 1982; Müller et al., 2008). Therefore, a relationship between CPO formation and slip-system activation would be expected even if it is not direct (Bascou et al., 2009; Karato et al., 2008; Katayama et al., 2005; Müller et al., 2008; Nagaya et al., 2014). The presence of CPO within a sample for post emplacement deformation, such as shock metamorphism, should therefore help contribute to the development of a dominant slip-system being activated within a given sample

through increasing the number of crystals oriented in a similar geometry with respect to the external strain field (Müller et al., 2008; Satsukawa & Michibayashi, 2009). Rocks, such as the nakhlites and other types of meteorites, which lack majority of the geological context used for terrestrial crystallographic deformation studies, such as sample orientation, require these larger datasets to begin to enable valid interpretations to be made from the data. We would even go so far as to insist that for samples such as meteorites slip-systems from multiple phases should be considered (where possible) to help counteract the lack of geological context and often the smaller amount of available sample for analysis before crystallographic slip-systems are used to infer extrinsic deformation parameters for a sample as opposed to a singular crystal.

4.2 The correlation between slip-system signature and deformation conditions observed in the nakhlites

In order to compare observed slip-systems in both olivine and augite (Figs. 14 and 15, Table 2) to deformation parameters, existing olivine diagrams (Fig. 16) have been modified and equivalent diagrams created for clinopyroxene (Fig. 17) using data from the literature. Note that the current extrinsic parameters presented in Figures 16 and 17 are based on low strain (*i.e.*, mantle induced) observations and experiments not naturally occurring specimens exposed to high strain rates such as the nakhlites. Studies assessing mantle olivine have shown that extrinsic parameters for slip-systems can be much lower in value for natural occurring samples compared to laboratory studies (Bernard et al., 2019) and references therein. It is therefore possible that the exact extrinsic parameters (axis values) stated for mantle augite and olivine in Figures 16 and 17 will be subject to change and may not be directly comparable to the presented data However, the positioning of each slip-system signature relative to one other will remain constant enabling the use of both Figure 16 and 17 in a more qualitative manner.

Comparison of slip-system signatures in laboratory studies for both clinopyroxene and olivine has shown that although there are preferred slip-systems activated along crystallographic planes under specific certain conditions within a given mineral (Avé Lallemant, 1978; Bystricky & Mackwell, 2001; Gueguen & Nicolas, 1980; Ingrin et al., 1991; Jaoul & Raterron, 1994; Kollé & Blacic, 1982; Zhang et al., 2006), a given slip plane is not necessarily tied to any specific set of universal extrinsic parameters. These identified extrinsic parameters are also not specifically transferrable to different minerals, even those that share the same crystal symmetry due to the contribution of intrinsic parameters. Thus, even if naturally occurring sample data were available to construct Figure 17 there would still be overlap in slip-system regions between Figures 16 and 17, where CPO has been activated in one mineral and not another. These regions of slip-system overlap could potentially lend towards the use of multiple mineral slip-systems to better refine deformation parameters, if the extrinsic parameter values were properly quantified for the sample (unlike the nakhlites presented here). Note that for Figure 17 there is currently not enough existing data regarding the effect of water content on clinopyroxene slip-system signatures to realistically discuss this intrinsic parameter for the here presented nakhlites. Thus, the presented results will only be discussed in terms of the external parameters: temperature and strain.

Variation between identified high and low deformation regions within the nakhlites identified from GROD angle maps suggest localisation of deformation within the nakhlites (*e.g.*, Fig. 5). The identification and localisation of mechanical twinning within identified high deformation regions suggest that the high deformation bands are related to shock deformation.

675 This interpretation is in line with observed mIPF slip-system patterns (discussed below) and
676 previous analysis of the nakhlites where shock levels were calculated to range between 5-20 GPa
677 (Fritz, Artemieva, et al., 2005).

678 *4.2.1 Impact deformation regime from mIPF slip-system patterns*

679 Similarities between whole section and high deformation region compared to low
680 deformation region mIPF slip-system patterns suggest that the localised high deformation
681 regions are more prevalent in the nakhlites than the low deformation region deformation source.
682 Out of the nine identified groups five express slip-system patterns more related to low
683 temperatures and high strain, while the other three (Groups V–VII, and IX) appear to be more
684 dominated by higher temperature deformation Figs 14, 16, and 17).

685 Within the mineral olivine the direction of slip along the {010} lattice plane tends to
686 respond the most significantly to temperature, whilst slip associated with either the {100} or
687 {001} lattice plane appear to respond more readily to changes in strain (Fig. 16). For the
688 nakhlites three of the six most commonly observed slip-system patterns are associated with
689 strain. Comparison between whole section, high deformation, and low deformation region results
690 show that these specific slip-systems, the most significant being {hk0}[001], is observed to
691 increase in intensity in the high deformation regions (Figs. 4, 14, and 15; Table 2).

692 Augite within the nakhlites is observed to deform preferentially in the direction of <001>
693 and <010> (Fig. 2). These preferences result in the commonly observed (100)[001] : (001)[100]
694 slip-system patterns (Fig. 2) identified at most Earth relevant temperature, pressure, stress, and
695 strain conditions (Fig. 17). This preferential occurrence in (100)[001] : (001)[100] slip-system
696 mIPF pattern matches observed crystallographic preferred orientation (CPO) patterns from
697 naturally occurring samples, where high levels of compression for <010> and perpendicular
698 alignment to the principal strain axis for <001> is observed (Frets et al., 2012; Mauler et al.,
699 2000). Experimental studies have shown the amount of (001)[100] slip present in a given sample
700 is observed to increase in response to greater amounts of strain at low temperatures (Fig. 17).
701 Between whole and high section mIPF results a slight increase in (001)[100] is observed within
702 some of the samples (*e.g.,* Fig. 12). Both groups I and II, encompassing eight of the 16 analysed
703 stones, exhibit mIPF patterns that relate increased proportions of (001)[100] slip within the
704 (100)[001] : (001)[100] pairing (Fig 14). When comparing between the high deformation and
705 low deformation regions, for all nakhlites exhibiting augite (100)[001]:(001)[100] mIPF slip-
706 system patterns, the intensity of (001)[100] is observed to decrease in the low deformation mIPF
707 plots (Fig. 15; Table 2). This indicates an increase in low temperature high strain deformation
708 being present within high deformation regions within the nakhlites.

709 Assessment of mIPF slip-system patterns suggest that impact deformation within the
710 nakhlites is typically expressed as {hk0}[001] slip in olivine and increased proportions of
711 (001)[100] within the (100)[001] : (001)[100] slip system pairing in augite (Figs 14 and 15).
712 However, it should be noted that the expression of impact induced deformation is not solely
713 restricted to the high GROD angle regions within a given nakhlite sample. Many of the low
714 deformation region mIPF slip-system patterns observed within the nakhlites still express
715 remnants of the low temperature, high strain slip (Fig. 15, Table 2).

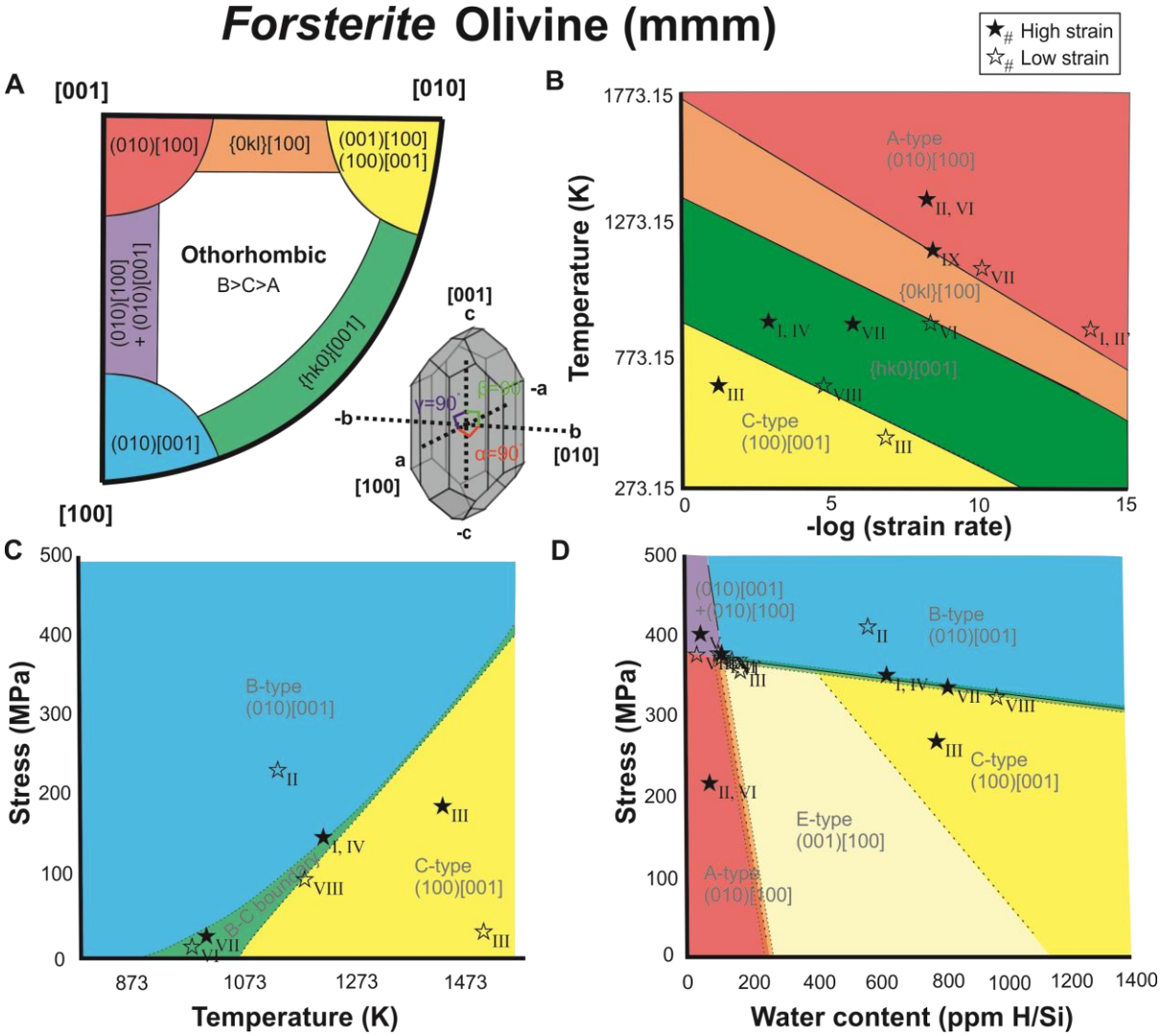

Figure 16. Known olivine (forsterite) slip-system deformation regions key (unit cells B>C>A). Colours indicate different slip-system regions. A) orthorhombic fundamental region slip-system key modified from (Ruzicka & Hugo, 2018) with a sketch of an olivine crystal illustrating its orthorhombic symmetry. B) Temperature vs. strain rate modified from (Katayama et al., 2004). C) Stress vs. Temperature modified from (Karato et al., 2008). D) Stress vs water content modified from (Karato et al., 2008). Note extrinsic parameters are based off low strain data. Note the placement of the identified nakhlite groupings (stars; Table 2) is only an indication of the related region and not absolute values.

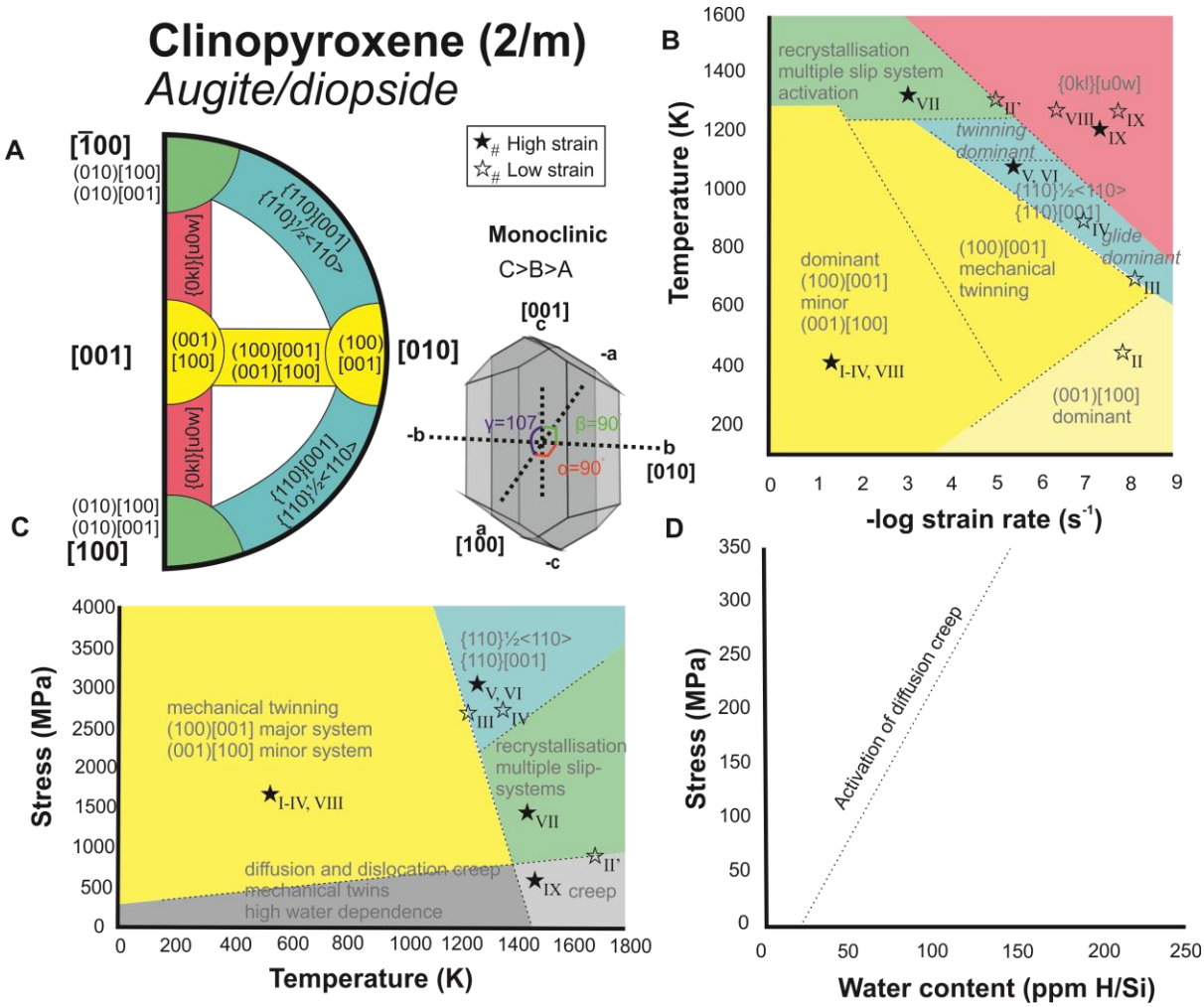

Figure 17. Proposed deformation conditions for clinopyroxene (augite/diopside) slip-systems key (unit cell C>B>A) based on experimental data. Colours indicate different slip-system regions. A) monoclinic fundamental region slip-system key for unit cell C>B>A with a sketch of an augite crystal illustrating its monoclinic symmetry. B) Temperature vs. strain rate (Avé Lallemant, 1978; Kollé & Blacic, 1982; Raleigh, 1967). C) Stress vs. Temperature (Avé Lallemant, 1978; Bystricky & Mackwell, 2001; Jaoul & Raterron, 1994; Kollé & Blacic, 1982; Müller et al., 2008; Zhang et al., 2006; Zhang & Green, 2007). D) Stress vs water content (Hier-Majumder et al., 2005). Due to the paucity of experimental data involving augite deformation in the presence of water, currently we can only state that there is a trend of lower extrinsic parameters required to induce the activation of specific slip-system signatures in augite with increased water content. Note extrinsic parameters are derived from low strain data. Note the placement of the identified nakhlite groupings (stars; Table 2) is only an indication of the related region and not absolute values.

4.2.2. Emplacement, low finite strain from mIPF slip-system pattern signatures

The occurrence of high deformation bands within the nakhlites in conjunction with their observed slip-system mIPF patterns indicating deformation related impact, suggests that the low deformation regions may provide evidence for emplacement deformation. Out of the 16 analysed

743 nakhlites, only four stones showed evidence for high temperature deformation within the high
744 deformation regions [Y 000749 (group V), MIL 090030 (group VI), MIL 090136 (Group VII),
745 and Y 000593 (127-A; group IX); Figs 9–11, and 13, respectively]. The high temperature slip-
746 system patterns observed in these regions were only seen to intensify in MUD values within the
747 low deformation regions mIPF plots (Figs. 14, 15). For augite slip in these groups is observed to
748 occur along the {110} lattice or along multiple slip planes (Fig. 2, 15, and 17) and for olivine slip
749 is predominantly observed to incorporate (010)[100] (Fig. 1, 14, and 16). It should be noted that
750 the samples attributed to groups V–VII, and IX all exhibited low detected GROD angles within
751 the map areas (Figs. 9–11, and 13). For identified groups I–IV, and VIII which all exhibit impact
752 related slip-system patterns had at least one analysed section within the group that exhibited
753 identifiable shifts in mIPF slip-system patterns between high and low deformation regions (Table
754 2). Assessment of the low deformation regions express mIPF slip-system patterns for those
755 sections show shifts that emphasise patterns related to (010)[001] or (001)[100]/(100)[001] in
756 olivine and (100)[001] in augite (Fig 15). (010)[100] slip is a common slip-system observed in
757 mantle olivine's on Earth (Fig. 16; (Bernard et al., 2019; Girard et al., 2013; Ohuchi et al., 2011;
758 Yao et al., 2019). The presence of (100)[001] slip in augite is also commonly observed within
759 nearly all naturally forming Earth samples (Bascou et al., 2002; Godard & van Roermund, 1995).
760 Ultimately the slip-system patterns observed within these samples are typically associated with
761 relatively low-moderate temperatures and low strain conditions (Figs. 16 and 17) indicating that
762 they are indeed remnants of emplacement deformation within the nakhlites that have been
763 subsequently overprinted by shock deformation.

764 *4.2.2. Dominant clinopyroxene slip-systems*

765 From the two analysed minerals augite shows the least diversity in mIPF slip-system
766 patterns (Table 2). Laboratory experiments have shown that clinopyroxene slip-systems are
767 strongly influenced by crystal orientation relative to the principal strain axis for the activation of
768 specific slip-systems (Avé Lallemant, 1978; Bascou et al., 2002; Kollé & Blacic, 1982).
769 Clinopyroxenes, including augite, have one of the lowest forms of crystal symmetry (monoclinic,
770 2/m). The relationship between augite's crystallographic axes (α = 107°, β =90°, and γ.= 90°),
771 where the crystallographic length of <c> > <a>, for augite's unit cell, will often require either
772 specific orientation and/or higher strain for activation of slip-systems other than (100)[001] :
773 (001)[100], such as {h0l} to form. Laboratory studies have also shown that even when such
774 specific conditions are met to activate another of augite's slip-systems, (100)[001] : (001)[100]
775 slip-systems will also often be observed within the sample (Ave Lallemant, 1978; Kollé &
776 Blacic, 1983; Philippot & van Roermund, 1992).

777 For any geological sample, a variety of observed different slip-systems within a single
778 sample would be expected. The expectation of variable slip-systems is in part due to the variation
779 in alignment of crystals within a given rock and each crystal's local petrological context and
780 surrounding mineral assemblage. For igneous samples, >50 % crystal alignment is considered as
781 strong fabric (Bunge, 1982; Vollmer, 1990). In the nakhlites, augite exhibits S- to LS-type fabric
782 where crystal alignment ranges from 8–26 % (Griffin et al., n.d.). The higher percentage of
783 random crystal orientations within any given sample coupled with a high dependence on crystal
784 orientation for the activation of slip-system signatures will naturally result in multiple slip-
785 system development between crystals. However, just like shape preferred orientation (SPO) and
786 CPO within a rock, in order to assess representative deformation across a given sample several

crystals preferentially on a similar level for statistical relevance (*i.e.*, ≥100–150 crystals) would need to be assessed (Skemer et al., 2005; Vollmer, 1990). Overall, despite the low crystal symmetry and higher slip-system activation criteria in clinopyroxenes, differences between certain extrinsic conditions, *e.g.*, low temperature and high pressure, high temperature low pressure, high temperature and pressure *etc.* can be observed (Fig. 17). However, studies so far indicate for most Earth relevant conditions the changes in slip-systems will be more subtle and be predominantly focused on shifts within the (100)[001] : (001)[100] slip-system pairing. Although clinopyroxene slip-systems have been identified to associate with specific conditions, there is a lot more work to be done. In particular, more information is needed addressing natural formation conditions and the effect of water content, before clinopyroxene slip-systems can be definitively used with the same level of certainty as geologists currently use olivine.

4.3 Implications for the nakhlites' time on Mars

Across the 16 analysed nakhlite meteorites nine distinct mIPF slip-system pattern combinations for whole section data are observed (Fig. 4) that reflect high strain deformation (Fig. 14). These mIPF slip-systems, when separated into respective high and low deformation regions (Figs, 14 and 15, Table 2), indicate signatures that most likely reflect differences in shock deformation. Even low deformation regions within the analysed nakhlites show a strong influence of high strain deformation (*e.g.*, shock) over low strain deformation signatures (*e.g.*, mantle). Hence the extrinsic parameters presented in Figures 16 and 17 will not be applicable to the nakhlites but the relationship between the different slip-systems can be applied. On this basis, the presented data show several different high-strain deformation environments from within the nakhlite source indicating heterogenous sampling of the ejection crater.

Comparison between whole section, high deformation, and low deformation region slip-system patterns across the 21 analysed sections show an increase in the slip-system patterns of {hk0}[001] in olivine and an increased (001)[100] component within the dominant augite (100)[001] : (001)[100] signature in high deformation regions. These particular slip-systems have been shown in mantle rocks to indicate increase strain at low temperatures (Figs. 16 and 17; Cordier, 2002; Katayama et al., 2004; Kollé & Blacic, 1983; Mainprice et al., 2005; Mauler et al., 2000), which suggests that this particular olivine-augite slip-system combination often expresses as the dominant or secondary slip-system pattern within the identified nakhlite groups, particularly groups I–IV and VIII (Figs. 5–9, 12–14, Table 2), could be indicative of shock-induced deformation. However, further investigations involving high strain experiments simulating hypervelocity impacts for both olivine and augite would be required to confirm if these slip-systems are preferentially activated during shock deformation processes or if they are in fact related to other low strain factors within the nakhlite source environment.

The establishment of olivine slip-systems under low-strain extrinsic parameters are well constrained where the influences of the extrinsic parameters are an ongoing and active field of research (Bernard et al., 2019). The relationship of augite to extrinsic parameters, on the other hand, has not been as consistently studied olivine but has gained serious momentum over the last decade [*e.g.*, Bascou et al. (2011), Tedonkenfack et al. (2021), and Van der Werf et al. (2017)]. Presented in this study is the first attempt to collate existing clinopyroxene slip-system data to begin thinking about clinopyroxene slip-systems in a similar manner to olivine with respect to extrinsic parameters. Through comparing observed clinopyroxene (in this instance augite) MIPF

slip-system patterns against published experimental data and the more-established olivine slip-system extrinsic parameters to ascertain patterns and commonalities (due to the data pertaining to low strain parameters), rough implications with respect to the nakhlites can be drawn. All of the identified groups apart from groups V–VII, and IX (Figs. 9–11, and 13, respectively; Table 2) exhibit slip-system patterns that are highly influenced by high strain deformation (Fig. 14, Table 2). Groups V–VII and IX express slip-system patterns commonly associated in mantle rocks with high temperature deformation the difference being group V exhibiting patterns indicative of higher strain and group IX indicating mIPF slip-system patterns potentially related to annealing processes (Figs. 9, 13, 16 and 17).

Separation of the high and low deformation regions within the nakhlites show that interpretation of mantle derived parameters is more complex than just assessing regions of low deformation within the samples. Despite the nakhlites being described as low shock samples [5–20 GPa (Fritz, Artemieva, et al., 2005; Fritz, Greshake, et al., 2005)], mIPF slip-system patterns even within the low deformation regions still exhibit weakened high deformation region signatures, most likely formed as the result of shock deformation (Fig. 15). This finding could support the hypothesis of the nakhlite ejecta crater being positioned on the extremity of an older crater (Daly et al., 2019). Out of all the analysed samples only 9 of the 21 sections showed significant shifts in either olivine and/or augite major mIPF slip-system patterns between separated high and low deformation regions (Table 2, Figs. 14 and 15). In these particular samples, an increase in the MUD is observed within less dominant mIPF slip-systems patterns and a weakening of the MUD for olivine {hk0}[001] and augite (001)[100] is typically observed. The implications of these observations indicate that there is potential for the minor slip-systems observed to increase in MUD intensity within the mIPF low deformation region plots could indicate nakhlite mantle related deformation. However, further investigation is required before any interpretations could be made.

The current groupings presented in Figures 4, 14, 15, and Table 2 indicate samples that share similar extrinsic parameters related to high strain deformation. This could be interpreted as samples exposed to similar conditions within the ejecta crater during launch. These groupings do not indicate that the samples are sourced from the same magmatic body as is evidence by samples MIL 03346 and NWA 817 within identified group II that show different slip-system patterns within their low deformation region mIPF plots despite sharing the same whole section and high deformation slip-system signatures (Table 2, Figs. 14 and 15). The same observation can be applied to the proposed ‘paired’ Yamato and Miller Range nakhlites were different mIPF slip-system patters are observed for both whole section (Fig. 4) and identified low and high deformation regions (Figs. 14 and 15, Table 2).

For the Yamato nakhlites, here categorised into groups I, V, VIII, and IX (Figs. 9, 12, and 13, Table 2) mIPF slip-system patterns express temperature differences that could not be resolved if they were located in the same position within the nakhlite ejecta crater and formed from the same magma body on Mars (Figs. 16 and 17). For the Miller Range nakhlites samples such as MIL 03346 and MIL 090032 could be related based off observed slip-system patterns (Figs. 6, 14, and 15, Table 2). However, both MIL 090030 (Fig. 10) and MIL 090030 (Fig. 11) exhibit mIPF slip-system patterns whose extrinsic parameters do not support pairing with any of the Miller Range nakhlites (Figs. 4, 14, and 15, Table 2).

Apart from the two Y 000593 sections, discussed above, each of the different Miller Range and Yamato samples are sourced from separate stones that were found in a similar location in Antarctica (Treiman, 2005). These locations are known glacial fields that are fed from a large catchment area. The variation observed in mIPF slip-system patterns between these 'paired' stones implies different deformation parameters for the separate meteorites, which could indicate either a range of deformation environments with each meteorite being sourced from a different section within the same igneous body or could suggest that each individual meteorite represents its own separate flow/intrusion. From rudimentary modelling of the nakhlite emplacement parameters, magma body unit thicknesses greater than ten meters were suggested for the Miller Range nakhlites, while the Yamato nakhlites were suggested to have magma body unit thicknesses less than ten meters (Griffin et al., n.d.). The smaller modelled unit thicknesses in conjunction with the observed differences in crystallographic deformation, similar recovery position, and geochronological dating (Cohen et al., 2017), currently supports the hypothesis that the Yamato individual nakhlites formed as individual igneous units that were located in close proximity to one another on Mars while the larger unit thicknesses, current geochronological dating in combination with presented crystallographic slip-systems would suggest that the Miller Range nakhlites could represent different regions (or lobes) from a single igneous event (Griffin et al., n.d.). Overall, variation in slip-system patterns observed from presented data, suggests that the suite of nakhlites meteorites heterogeneously sample different areas from within their launch crater on Mars, sampling a variety of different igneous units.

5 Conclusions

Observed slip-system patterns can be used to discern between samples exposed to varying extrinsic parameters. However, more work (both natural samples and laboratory based) needs to be undertaken to further constrain slip-system signature extrinsic parameters, particularly regarding the effects of high strain and water content. In addition, large area EBSD has the potential to become a powerful technique to constrain extrinsic parameters associated with deformation (*i.e.*, pressure, temperature, strain, water content) of Martian magmas and other meteorites when combined with analysis of naturally occurring samples and laboratory experiments regarding slip-system activations.

Combined olivine and clinopyroxene mIPF slip-system patterns identified nine different slip-system pattern combinations within the nakhlites five of which were associated with high strain deformation interpreted as shock deformation. This shock (high strain) deformation is observed as increased proportions of (001)[100] in augite and {hk0}[001] in olivine. Investigation of slip-system patterns between identified high and low deformation regions within the data indicate high strain deformation to be prevalent through the sample, including within the low deformation regions. Less dominant slip-system patterns identified to increase in MUD intensity within the low deformation slip-system patterns could have the potential to represent low strain (mantle related) deformation. However, further work investigating the contributions of shock metamorphism and the exact relationship between high strain slip-system extrinsic parameters is required.

Acknowledgments, Samples, and Data

For providing the samples used in this study we thank the NHM London, Japanese Antarctic Meteorite Research Centre, Smithsonian, NASA Meteorite Working Group, Macovich Collection, The Museum of Western Australia, Centre Européen de Recherche et d'Enseignemet de Géosciences de l'Environment (CEREGE), and the Institute of Meteoritics University of New Mexico. This work was funded by the Science and Technology Facilities Council through grants ST/N000846/1 and ST/H002960/1 to M.R.L). All data are available at DOI:10.5281/zenodo.5545821.

References

Ashby, M. F. (1970). The deformation of plastically non-homogeneous materials. *Philosophical Magazine*, *21*(170), 399–424. https://doi.org/10.1080/14786437008238426

Ashby, M. F. (1983). *Mechanisms of Deformation and Fracture*. *Advances in Applied Mechanics* (Vol. 23).

Avé Lallemant, H. G. (1978). Experimental deformation of diopside and websterite. *Tectonophysics*, *48*(1–2), 1–27. https://doi.org/10.1016/0040-1951(78)90083-5

Ave Lallemant, H. G. A. (1978). Experimental deformation of diopside and websterite. *Tectonophysics*, *48*, 1–27.

Barber, D. J., Wenk, H. R., Hirth, G., & Kohlstedt, D. L. (2010). *Chapter 95 Dislocations in Minerals*. *Dislocations in Solids* (Vol. 16). Elsevier. https://doi.org/10.1016/S1572-4859(09)01604-0

Bascou, J., Tommasi, A., & Mainprice, D. (2002). Plastic deformation and development of clinopyroxene lattice preferred orientations in eclogites. *Journal of Structural Geology*, *24*, 1357–1368.

Bascou, J., Tommansi, A., & Mainprice, D. (2009). Plastic deformation and development of clinopyroxene lattice preferred orientations in eclogites. *Journal of Structural Geology*, *24*(2002), 43603.

Bascou, J., Doucet, L. S., Saumet, S., Ionov, D. A., Ashchepkov, I. V., & Golovin, A. V. (2011). Seismic velocities, anisotropy and deformation in Siberian cratonic mantle: EBSD data on xenoliths from the Udachnaya kimberlite. *Earth and Planetary Science Letters*, *304*(1–2), 71–84. https://doi.org/10.1016/j.epsl.2011.01.016

Bernard, R. E., Behr, W. M., Becker, T. W., Young, D. J., & Young, David, J. (2019). Relationships Between Olivine CPO and Deformation Parameters in Naturally Deformed Rocks and Implications for Mantle Seismic Anisotropy. *Geochemistry, Geophysics, Geosystems*, *20*(7), 3469–3494. https://doi.org/10.1029/2019GC008289

Boneh, Y., & Skemer, P. (2014). The effect of deformation history on the evolution of olivine CPO. *Earth and Planetary Science Letters*, *406*, 213–222. https://doi.org/10.1016/j.epsl.2014.09.018

Bunch, T. E., & Reid, A. M. (1975). The Nakhlites. Part I: Petrography and mineral chemistry. *Meteoritics*, *10*, 303–315.

Bunge, H.-J. (1982). *Texture analysis in materials science: Mathematical methods*. (H.-J. Bunge, Ed.) (Paperback). Cuvillier Verlag, Gottingen. https://doi.org/10.7312/chi-18840-001

Bystricky, M., & Mackwell, S. (2001). Creep of dry clinopyroxene aggregates with deformation in the dislocation creep. *Journal of Geophysical Research*, *106*, 13443–13454.

Cohen, B. E., Mark, D. F., Cassata, W. S., Lee, M. R., Tomkinson, T., Smith, C. L., et al. (2017). Taking the pulse of Mars via dating of a plume-fed volcano. *Nature Communications*, *8*(1), 640. https://doi.org/10.1038/s41467-017-00513-8

Cordier, P. (2002). Dislocations and slip systems of mantle minerals. *Reviews in Mineralogy and Geochemistry*, *51*. https://doi.org/10.2138/gsrmg.51.1.137

Corrigan, C. M., Velbel, M. A., & Vicenzi, E. P. (2015). Modal abundances of pyroxene, olivine, and mesostasis in nakhlites: Heterogeneity, variation, and implications for nakhlite emplacement. *Meteoritics and Planetary Science*, *50*(9), 1497–1511. https://doi.org/10.1111/maps.12492

Daly, L., Lee, M. R., Piazolo, S., Griffin, S., Bazargan, M., Campanale, F., et al. (2019). Boom Boom Pow: shock-facilitated aquesous alteration and evidence for two shock events in the Martian nakhlite meteorites. *Science Advances*, *5*(9), 1-11/eaaw5549. https://doi.org/DOI: 10.1126/sciadv.aaw5549

Day, J. M. D., Tait, K. T., Udry, A., Moynier, F., Liu, Y., & Neal, C. R. (2018). Martian magmatism from plume metasomatized mantle. *Nature Communications*, *9*(1), 4799. https://doi.org/10.1038/s41467-018-07191-0

Farla, R. J. M., Kokkonen, H., Gerald, J. D. F., Barnhoorn, A., Faul, U. H., & Jackson, I. (2011). Dislocation recovery in fine-grained polycrystalline olivine. *Physics and Chemistry of Minerals*, *38*(5), 363–377.

https://doi.org/10.1007/s00269-010-0410-3
Fei, H., Hegoda, C., Yamazaki, D., Wiedenbeck, M., Yurimoto, H., Shcheka, S., & Katsura, T. (2012). High silicon self-diffusion coefficient in dry forsterite. *Earth and Planetary Science Letters*, *345–348*, 95–103. https://doi.org/10.1016/j.epsl.2012.06.044
Fleck, N. A., Muller, G. M., Ashby, M. F., & Hutchinson, J. W. (1994). Strain gradient plasticity :theory and experiment, acta metal material. *Acta Metal Material*, *42*(2), 475–487.
Frets, E., Tommasi, A., Garrido, C. J., Padrón-Navarta, J. A., Amri, I., & Targuisti, K. (2012). Deformation processes and rheology of pyroxenites under lithospheric mantle conditions. *Journal of Structural Geology*, *39*, 138–157. https://doi.org/10.1016/j.jsg.2012.02.019
Friedrich, J. M., Ruzicka, A., Macke, R. J., Thostenson, J. O., Rudolph, R. A., Rivers, M. L., & Ebel, D. S. (2017). Relationships among physical properties as indicators of high temperature deformation or post-shock thermal annealing in ordinary chondrites. *Geochimica et Cosmochimica Acta*, *203*, 157–174. https://doi.org/10.1016/j.gca.2016.12.039
Fritz, J., Artemieva, N. A., & Greshake, A. (2005). Ejection of Martian meteorites. *Meteoritics & Planetary Science*, *40*(9–10), 1393–1411. https://doi.org/10.1111/j.1945-5100.2005.tb00409.x
Fritz, J., Greshake, A., & Stöffler, D. (2005). Micro-Ramen spectroscopy of plagioclase and maskelynite in Martian meteorites: Evidence of progressive shock metamorphism. *Antarctic Meteorite Research*, *18*, 96–116.
Girard, J., Chen, J., Raterron, P., & Holyoke, C. W. (2013). Hydrolytic weakening of olivine at mantle pressure: Evidence of [100](010) slip system softening from single-crystal deformation experiments. *Physics of the Earth and Planetary Interiors*, *216*, 12–20. https://doi.org/10.1016/j.pepi.2012.10.009
Godard, G., & van Roermund, H. L. M. (1995). Deformation-induced clinopyroxene fabrics from eclogites. *Journal of Structural Geology*, *17*(10), 1425–1443. https://doi.org/10.1016/0191-8141(95)00038-F
Griffin, S., Keller, T., Daly, L., Lee, M. R., Cohen, B. E., Forman, L. V., et al. (n.d.). *Emplacement of Amazonian nakhlite ignenous rocks and implications for their source volcano on Mars*.
Groves, G. W., & Kelly, A. (1963). Independent slip systems in crystals. *Philosophical Magazine*, *8*(89), 877–887. https://doi.org/10.1080/14786436308213843
Gueguen, Y., & Nicolas, A. (1980). Deformation of mantle rocks. *Annual Review of Earth and Planetary Sciences*, *8*, 119–144.
Hallis, L. J., & Taylor, G. J. (2011). Comparisons of the four Miller Range nakhlites, MIL 03346, 090030, 090032 and 090136: Textural and compositional observations of primary and secondary mineral assemblages. *Meteoritics and Planetary Science*, *46*(12), 1787–1803. https://doi.org/10.1111/j.1945-5100.2011.01293.x
Hansen, L. N., Zhao, Y. H., Zimmerman, M. E., & Kohlstedt, D. L. (2014). Protracted fabric evolution in olivine: Implications for the relationship among strain, crystallographic fabric, and seismic anisotropy. *Earth and Planetary Science Letters*, *387*, 157–168. https://doi.org/10.1016/j.epsl.2013.11.009
Henry, H., Tilhac, R., Griffin, W. L., O'Reilly, S. Y., Satsukawa, T., Kaczmarek, M.-A., et al. (2017). Deformation of mantle pyroxenites provides clues to geodynamic processes in subduction zones: Case study of the Cabo Ortegal Complex, Spain. *Earth and Planetary Science Letters*, *472*, 174–185. https://doi.org/10.1016/j.epsl.2017.05.028
Hier-Majumder, S., Mei, S., & Kohlstedt, D. L. (2005). Water weakening of clinopyroxenite in diffusion creep. *Journal of Geophysical Research: Solid Earth*, *110*(7), 1–12. https://doi.org/10.1029/2004JB003414
Hunter, R. H. (1996). Texture Development in Cumulate Rocks. *Developments in Petrology*, *15*(C), 77–101. https://doi.org/10.1016/S0167-2894(96)80005-4
Imae, N., Ikeda, Y., & Kojima, H. (2005). Petrology of the Yamato nakhlites. *Meteoritics and Planetary Science*, *40*(11), 1581–1598. https://doi.org/10.1111/j.1945-5100.2005.tb00133.x
Ingrin, J., Doukhan, N., & Doukhan, J. C. (1991). High-Temperature Deformation of Diopside Single-Crystal .2. Transmission Electron-Microscopy Investigation Of The Defect Microstructures. *Journal Of Geophysical Research-Solid Earth And Planets*, *96*(B9), 14287–14297. https://doi.org/10.1029/91JB01233
Jaoul, O., & Raterron, P. (1994). High-temperature deformation of diopside crystal 3. Influences of pO2 and SiO2 precipitation. *Journal of Geophysical Research*, *99*(B5), 9423–9439. https://doi.org/10.1029/93JB03363
Jung, H., Katayama, I., Jiang, Z., Hiraga, T., & Karato, S.-I. (2006). Effect of water and stress on the lattice-preferred orientation of olivine. *Tectonophysics*, *421*(1–2), 1–22. https://doi.org/10.1016/j.tecto.2006.02.011
Jung, Haemyeong, Mo, W., & Green, H. W. (2009). Upper mantle seismic anisotropy resulting from pressure-induced slip transition in olivine. *Nature Geoscience*, *2*(1), 73–77. https://doi.org/10.1038/ngeo389
Kaboli, S., Burnley, P. C., Xia, G., & Green, H. W. (2017). Pressure Dependence of Creep in Forsterite Olivine: Comparison of Measurements From the D-DIA and Griggs Apparatus. *Geophysical Research Letters*, *44*(21), 10,939-10,947. https://doi.org/10.1002/2017GL075177

Karato, S., Jung, H., Katayama, I., & Skemer, P. (2008). Geodynamic Significance of Seismic Anisotropy of the Upper Mantle: New Insights from Laboratory Studies. *Annual Review of Earth and Planetary Sciences*, *36*(1), 59–95. https://doi.org/10.1146/annurev.earth.36.031207.124120

Katayama, I., & Karato, S. ichiro. (2006). Effect of temperature on the B- to C-type olivine fabric transition and implication for flow pattern in subduction zones. *Physics of the Earth and Planetary Interiors*, *157*(1–2), 33–45. https://doi.org/10.1016/j.pepi.2006.03.005

Katayama, I., Jung, H., & Karato, S. I. (2004). New type of olivine fabric from deformation experiments at modest water content and low stress. *Geology*, *32*(12), 1045–1048. https://doi.org/10.1130/G20805.1

Katayama, I., Karato, S. I., & Brandon, M. (2005). Evidence of high water content in the deep upper mantle inferred from deformation microstructures. *Geology*, *33*(7), 613–616. https://doi.org/10.1130/G21332.1

Keppler, R. (2018). Crystallographic preferred orientations in eclogites – A review. *Journal of Structural Geology*, *115*(April), 284–296. https://doi.org/10.1016/j.jsg.2018.04.003

Kollé, J. J., & Blacic, J. D. (1982). Deformation of single-crystal clinopyroxenes: 1. Mechanical twinning in diopside and hedenbergite. *Journal of Geophysical Research*, *87*(B5), 4019–4034.

Kollé, J. J., & Blacic, J. D. (1983). Deformation of single-crystal clinopyroxenes: 2. Dislocation- controlled flow processes in hedenbergite. *Journal of Geophysical Research*, *88*(B3), 2381–2393. https://doi.org/10.1029/JB088iB03p02381

Krämer Ruggiu, L., Gattacceca, J., Bevouard, B., Udry, A., Debaille, V., Rochette, P., et al. (2020). Caleta el Cobre 022 martian meteorite: increasing nakhlite diversity. *Meteoritics and Planetary Science*, *25*, 1–25. https://doi.org/10.1111/maps.13534

Law, R. D. (1990). Crystallographic fabrics: a selective review of their applications to research in structural geology. *Deformation Mechanisms, Rheology and Tectonics. Geological Society Special Publication*, *54*(54), 352–355. https://doi.org/10.1144/GSL.SP.1990.054.01.30

Lee, M. R., Tomkinson, T., Hallis, L. J., & Mark, D. F. (2015). Formation of iddingsite veins in the martian crust by centripetal replacement of olivine: Evidence from the nakhlite meteorite Lafayette. *Geochimica et Cosmochimica Acta*, *154*, 49–65. https://doi.org/10.1016/j.gca.2015.01.022

Li, Z. Y., Wen, D. P., Wang, Y. F., & Liu, X. (2020). An Investigation of Dislocation in Olivine Phenocrysts from the Hawaiian Basalts. *Journal of Earth Science*, *31*(6), 1183–1189. https://doi.org/10.1007/s12583-020-1338-2

Liu, S., Tommasi, A., Vauchez, A., & Mazzucchelli, M. (2019). Deformation, Annealing, Melt-Rock Interaction, and Seismic Properties of an Old Domain of the Equatorial Atlantic Lithospheric Mantle. *Tectonics*, *38*(4), 1164–1188. https://doi.org/10.1029/2018TC005373

Mainprice, D., Tommasi, A., Couvy, H., Cordier, P., & Frost, D. J. (2005). Pressure sensitivity of olivine slip systems and seismic anisotropy of Earth's upper mantle. *Nature*, *433*(7027), 731–733. https://doi.org/10.1038/nature03266

Mainprice, D., Bachmann, F., Hielscher, R., & Schaeben, H. (2015). Descriptive tools for the analysis of texture projects with large datasets using MTEX: Strength, symmetry and components. *Geological Society Special Publication*, *409*(1), 251–271. https://doi.org/10.1144/SP409.8

Mauler, A., Bystricky, M., Kunze, K., & Mackwell, S. (2000). Microstructures and lattice preferred orientations in experimentally deformed clinopyroxene aggregates. *Journal of Structural Geology*, *22*, 1633–1648. https://doi.org/10.1016/S0191-8141(00)00073-0

Mei, S., & Kohlstedt, D. L. (2000). Influence of water on plastic deformation of olivine aggregates 2. Dislocation creep regime. *Journal of Geophysical Research: Solid Earth*, *105*(B9), 21471–21481. https://doi.org/10.1029/2000jb900180

Müller, W. F., Walte, N., & Miyajima, N. (2008). Experimental deformation of ordered natural omphacite: a study by transmission electron microscopy. *European Journal of Mineralogy*, *20*, 835–844. https://doi.org/10.1127/0935-1221/2008/0020-1851

Muto, J., Hirth, G., Heilbronner, R., & Tullis, J. (2011). Plastic anisotropy and fabric evolution in sheared and recrystallized quartz single crystals. *Journal of Geophysical Research: Solid Earth*, *116*(2), 1–18. https://doi.org/10.1029/2010JB007891

Nagaya, T., Wallis, S. R., Kobayashi, H., Michibayashi, K., Mizukami, T., Seto, Y., et al. (2014). Dehydration breakdown of antigorite and the formation of B-type olivine CPO. *Earth and Planetary Science Letters*, *387*, 67–76. https://doi.org/10.1016/j.epsl.2013.11.025

Noguchi, T., Nakamura, T., Misawa, K., Imae, N., Aoki, T., & Toh, S. (2009). Laihunite and jarosite in the Yamato 00 nakhlites: Alteration products on Mars? *Journal of Geophysical Research: Planets*, *114*(10), 1–13. https://doi.org/10.1029/2009JE003364

Ohuchi, T., Kawazoe, T., Nishihara, Y., Nishiyama, N., & Irifune, T. (2011). High pressure and temperature fabric transitions in olivine and variations in upper mantle seismic anisotropy. *Earth and Planetary Science Letters*, *304*(1–2), 55–63. https://doi.org/10.1016/j.epsl.2011.01.015

Philippot, P., & van Roermund, H. L. M. (1992). Deformation processes in eclogitic rocks: evidence for the rheological delamination of the oceanic crust in deeper levels of subduction zones. *Journal of Structural Geology*, *14*(8/9), 1059–1077. https://doi.org/10.1016/0191-8141(92)90036-V

Poirier, J.-P. (1975). On the Slip Systems of Olivine. *Journal of Geophysical Research*, *80*(29), 4059–4061.

Poirier, J.-P. (1982). On transformation plasticity. *Journal of Geophysical Research*, *87*(B8), 6791–6797.

Poirier, J.-P. (1985). *Creep of crystals: High-temperature deformation processes in Metals, ceramics and minerals*. Cambridge University Press.

Poirier, J.-P. (1995). Mineral physics and. In T. J. Ahrens (Ed.), *Mineral physics and crystallography: a handbook of physical constants* (pp. 245–252). American Geophysical Union. https://doi.org/10.4324/9780203121146-35

Poirier, J.-P., & Nicolas, A. (1975). Deformation-Induced Recrystallization Due to Progressive Misorientation of Subgrains, with Special Reference to Mantle Peridotites. *The Journal of Geology*, *83*(6), 707–720. https://doi.org/10.1086/628163

Précigout, J., & Hirth, G. (2014). B-type olivine fabric induced by grain boundary sliding. *Earth and Planetary Science Letters*, *395*, 231–240. https://doi.org/10.1016/j.epsl.2014.03.052

Qi, C., Hansen, L. N., Wallis, D., Holtzman, B. K., & Kohlstedt, D. L. (2018). Crystallographic Preferred Orientation of Olivine in Sheared Partially Molten Rocks: The Source of the "a-c Switch." *Geochemistry, Geophysics, Geosystems*, *19*(2), 316–336. https://doi.org/10.1002/2017GC007309

Raleigh, C. B. (1967). Plastic Deformation of Upper Mantle Silicate Minerals. *Geophysical Journal of the Royal Astronomical Society*, *14*, 45–49. https://doi.org/10.1111/j.1365-246X.1967.tb06220.x

Raterron, P., Doukhan, N., Jaoul, O., & Doukhan, J. C. (1994). High temperature deformation of diopside IV: predominance of {110} glide above 1000°C. *Physics of the Earth and Planetary Interiors*, *82*, 209–222. https://doi.org/10.1016/0031-9201(94)90073-6

Raterron, Paul, & Jaoul, O. (1991). High-temperature deformation of diopside single crystal: 1. Mechanical data. *Journal of Geophysical Research: Solid Earth*, *96*(B9), 14277–14286. https://doi.org/10.1029/91JB01205

Raterron, Paul, Chen, J., Geenen, T., & Girard, J. (2011). Pressure effect on forsterite dislocation slip systems: Implications for upper-mantle LPO and low viscosity zone. *Physics of the Earth and Planetary Interiors*, *188*(1–2), 26–36. https://doi.org/10.1016/j.pepi.2011.06.009

van Roermund, H. L. M., & Boland, J. N. (1981). The dislocation substructures of naturally deformed omphacites. *Tectonophysics*, *78*, 403–418.

Ruggles, T. J., & Fullwood, D. T. (2013). Estimations of bulk geometrically necessary dislocation density using high resolution EBSD. *Ultramicroscopy*, *133*, 8–15. https://doi.org/10.1016/j.ultramic.2013.04.011

Ruzicka, A. M., & Hugo, R. C. (2018). Electron backscatter diffraction (EBSD) study of seven heavily metamorphosed chondrites: Deformation systematics and variations in pre-shock temperature and post-shock annealing. *Geochimica et Cosmochimica Acta*, *234*, 115–147. https://doi.org/10.1016/j.gca.2018.05.014

Satsukawa, T., & Michibayashi, K. (2009). Determination of slip system in olivine based on crystallographic preferred orientation and subgrain-rotation axis: examples from Ichinomegata peridotite xenoliths, Oga peninsula, Akita prefecture. *The Journal of the Geological Society of Japan*, *115*(6), 288–291. https://doi.org/10.5575/geosoc.115.288

Sciences, P. (1978). The mechanisms of creep in olivine. *Philosophical Transactions of the Royal Society of London. Series A, Mathematical and Physical Sciences*, *288*(1350), 99–119. https://doi.org/10.1098/rsta.1978.0008

Skemer, P., Katayama, I., Jiang, Z., & Karato, S. I. (2005). The misorientation index: Development of a new method for calculating the strength of lattice-preferred orientation. *Tectonophysics*, *411*(1–4), 157–167. https://doi.org/10.1016/j.tecto.2005.08.023

Skrotzki, W. (1994). Defect structure and deformation mechanisms in naturally deformed augite and enstatite. *Tectonophysics*, *229*(1–2), 43–68. https://doi.org/10.1016/0040-1951(94)90005-1

Soustelle, V., & Manthilake, G. (2017). Deformation of olivine-orthopyroxene aggregates at high pressure and temperature: Implications for the seismic properties of the asthenosphere. *Tectonophysics*, *694*, 385–399. https://doi.org/10.1016/j.tecto.2016.11.020

Stocker, R. L., & Ashby, M. F. (1973). On the rheology of the upper mantle. *Reviews of Geophysics and Space Physics*, *11*(2), 391–426.

Stöffler, D., Hamann, C., & Metzler, K. (2018). Shock metamorphism of planetary silicate rocks and sediments:

Proposal for an updated classification system. *Meteoritics and Planetary Science*, *53*(1), 5–49. https://doi.org/10.1111/maps.12912

Sundberg, M., & Cooper, R. F. (2008). Crystallographic preferred orientation produced by diffusional creep of harzburgite: Effects of chemical interactions among phases during plastic flow. *Journal of Geophysical Research: Solid Earth*, *113*(12), 1–16. https://doi.org/10.1029/2008JB005618

Tasaka, M., Michibayashi, K., & Mainprice, D. (2008). B-type olivine fabrics developed in the fore-arc side of the mantle wedge along a subducting slab. *Earth and Planetary Science Letters*, *272*(3–4), 747–757. https://doi.org/10.1016/j.epsl.2008.06.014

Tedonkenfack, S. S. T., Puziewicz, J., Aulbach, S., Ntaflos, T., Kaczmarek, M. A., Matusiak-Małek, M., et al. (2021). Lithospheric mantle refertilization by DMM-derived melts beneath the Cameroon Volcanic Line—a case study of the Befang xenolith suite (Oku Volcanic Group, Cameroon). *Contributions to Mineralogy and Petrology*, *176*(5), 1–18. https://doi.org/10.1007/s00410-021-01796-3

Treiman, A. H. (2005). The nakhlite meteorites: Augite-rich igneous rocks from Mars. *Chemie Der Erde - Geochemistry*, *65*(3), 203–270. https://doi.org/10.1016/j.chemer.2005.01.004

Udry, A., & Day, J. M. D. (2018). 1.34 billion-year-old magmatism on Mars evaluated from the co-genetic nakhlite and chassignite meteorites. *Geochimica et Cosmochimica Acta*, *238*, 292–315. https://doi.org/10.1016/J.GCA.2018.07.006

Udry, A., Howarth, G. H., Herd, C., Day, J. M. D., Lapen, T. J., & Filiberto, J. (2020). What martian meteorites reveal about the interior and surface of Mars. *Journal of Geophysical Research: Planets*, *125*, e2020JE006523. https://doi.org/10.1029/2020JE006523

Ulrich, S., & Mainprice, D. (2005). Does cation ordering in omphacite influence development of lattice-preferred orientation? *Journal of Structural Geology*, *27*(3), 419–431. https://doi.org/10.1016/j.jsg.2004.11.003

Vollmer, F. W. (1990). An application of eigenvalue methods to structural domain analysis. *Bulletin of the Geological Society of America*, *102*(6), 786–791. https://doi.org/10.1130/0016-7606(1990)102<0786:AAOEMT>2.3.CO;2

Watt, L. E., Bland, P. A., Prior, D. J., & Russell, S. S. (2006). Fabric analysis of Allende matrix using EBSD. *Meteoritics and Planetary Science*, *41*(7), 989–1001. https://doi.org/10.1111/j.1945-5100.2006.tb00499.x

Wenk, H.-R., & Tomé, C. N. (1999). Modeling dynamic recrystallization of olivine aggregates deformed in simple shear. *Journal of Geophysical Research: Solid Earth*, *104*(B11), 25513–25527. https://doi.org/10.1029/1999jb900261

Van Der Werf, T., Chatzaras, V., Marcel Kriegsman, L., Kronenberg, A., Tikoff, B., & Drury, M. R. (2017). Constraints on the rheology of the lower crust in a strike-slip plate boundary: Evidence from the San Quintín xenoliths, Baja California, Mexico. *Solid Earth*, *8*(6), 1211–1239. https://doi.org/10.5194/se-8-1211-2017

Winiarski, B., Gholinia, A., Mingard, K., Gee, M., Thompson, G., & Withers, P. J. (2021). Correction of artefacts associated with large area EBSD. *Ultramicroscopy*, *226*(March), 113315. https://doi.org/10.1016/j.ultramic.2021.113315

Woodward, C. (2005). Plasticity at the Atomic Scale: Parametric, Atomistic, and Electronic Structure Methods. *Handbook of Materials Modeling*, 2865–2869. https://doi.org/10.1007/978-1-4020-3286-8_171

Yao, Z., Qin, K., Wang, Q., & Xue, S. (2019). Weak B-Type Olivine Fabric Induced by Fast Compaction of Crystal Mush in a Crustal Magma Reservoir. *Journal of Geophysical Research: Solid Earth*, *124*(4), 3530–3556. https://doi.org/10.1029/2018JB016728

Zhang, J., & Green, H. W. (2007). Experimental investigation of eclogite rheology and its fabrics at high temperature and pressure. *Journal of Metamorphic Geology*, *25*, 97–115. https://doi.org/10.1111/j.1525-1314.2006.00684.x

Zhang, J., Green II, H. W., & Bozhilov, K. N. (2006). Rheology of omphacite at high temperature and pressure and significance of its lattice preferred orientations. *Earth and Planetary Science Letters*, *246*, 432–443. https://doi.org/10.1016/j.epsl.2006.04.006